REPORT

FERROELECTRICS

Super-elastic ferroelectric single-crystal membrane with continuous electric dipole rotation

Guohua Dong[1]*, Suzhi Li[2]*, Mouteng Yao[1]*, Ziyao Zhou[1]†, Yong-Qiang Zhang[3], Xu Han[4], Zhenlin Luo[4], Junxiang Yao[5], Bin Peng[1], Zhongqiang Hu[1], Houbing Huang[6], Tingting Jia[5], Jiangyu Li[5], Wei Ren[1], Zuo-Guang Ye[7], Xiangdong Ding[2]†, Jun Sun[2], Ce-Wen Nan[8], Long-Qing Chen[9], Ju Li[10], Ming Liu[1]†

Ferroelectrics are usually inflexible oxides that undergo brittle deformation. We synthesized freestanding single-crystalline ferroelectric barium titanate ($BaTiO_3$) membranes with a damage-free lifting-off process. Our $BaTiO_3$ membranes can undergo a ~180° folding during an in situ bending test, demonstrating a super-elasticity and ultraflexibility. We found that the origin of the super-elasticity was from the dynamic evolution of ferroelectric nanodomains. High stresses modulate the energy landscape markedly and allow the dipoles to rotate continuously between the *a* and *c* nanodomains. A continuous transition zone is formed to accommodate the variant strain and avoid high mismatch stress that usually causes fracture. The phenomenon should be possible in other ferroelectrics systems through domain engineering. The ultraflexible epitaxial ferroelectric membranes could enable many applications such as flexible sensors, memories, and electronic skins.

Elasticity reflects the capability of a material to exhibit mechanical deformation and recovery. Elasticity and flexibility of material such as alloys and semiconductors are determined by the essential components (atoms and molecules, among others) and their interactions (chemical bonds) in the materials. In metals, elasticity originates from free transfer among electron components without changing the Fermi level substantially during mechanic deformation (*1*). Some alloys called shape-memory alloys can even achieve the shape recoverability with strain exceeding the elastic limit through the martesitic phase transition, leading to the super-elasticity (*2*). By contrast, the ionic or covalence bonds in oxides and semiconductors have much greater interaction strength but lack sufficient slip systems for dislocation movement under deformation, leading to a brittle fracture. Nevertheless, the phase transitions in nanostructural oxides and semiconductors with reduction in dimensionality (*3*–*5*) offer atomic displacement tolerance in coexisted phases (*6*) and trigger additional strain that exceeds the elastic limit of bulk materials and has the ability for recovery.

Ferroelectrics (FEs), as a class of functional oxides, have found broad applications due to the existence of switchable spontaneous polarization and its coupling to mechanic deformation. Flexible FE thin films and membranes are needed for advanced flexible FE electronics, which will fulfill the growing demands for applications (*7*–*9*). In recent years, novel peeling and transferring technologies developed for oxide thin films have provided a step forward toward fabricating high-quality epitaxial membranes (*10*–*15*). However, little has been done in investigating the presence, origin, and limit of elasticity and flexibility in FE thin films and membranes. This is an important topic pertinent to various research areas such as flexoelectricity and multiferroics, in which strong electrical-mechanical coupling effects can be generated through large bending deformation. Although the ionic or covalence bonds in FEs constrain the elasticity in general, the FE domain evolution could provide an alternative avenue to complete the super-elasticity in oxides instead of phase transformations. For example, perovskite $BaTiO_3$ (BTO) films (tetragonal phase), a classic FE and piezoelectric material, usually contain both *a* and *c* domains (*16*, *17*). The transition between these *a* and *c* domains may enable shape tolerability during the bending process.

We synthesized BTO/$Sr_3Al_2O_6$ (SAO) heterostructures by means of pulsed-laser deposition on (001) $SrTiO_3$ (STO) substrates (*18*). The samples were immersed in the deionized water to dissolve the sacrificial SAO layer to obtain freestanding BTO membranes (*10*). The synchrotron-based reciprocal space mapping (RSM) around the pseudocubic (002) and (103) reflections confirms the heteroepitaxial growth of the BTO (60 nm)/SAO film (Fig. 1B). We confirmed the *c* axis–oriented BTO/SAO heterostructure with the θ to 2θ pattern (fig. S1). We found the BTO showed a tetragonal phase with c/a = 1.024 and possessed along an out-of-plane polarization. The RSM pattern around the (002) and (103) peaks presented single-crystal characteristics in flexible BTO/polydimethylsiloxane (PDMS). We recorded a wide range of thicknesses for the RSM of films (figs. S2 and S3). We used scanning electron microscopy (SEM) and atomic force microscopy (AFM) to determine the surface morphology and roughness of the large-scale transferred BTO membrane (fig. S4).

We transferred large-area freestanding single-crystal BTO membranes onto a Cu grid with lacey carbon film. We imaged the 50-nm BTO membrane with a low-magnification plan-view scanning transmission electron microscopy (STEM) and atomic resolution high angle annular dark field (HAADF) STEM image (Fig. 1G). We also imaged freestanding and cross-sectional membranes (figs. S5 to S7). Under the irradiation of an electron beam, the freestanding BTO membrane looks like a translucent plastic layer on the porous carbon frame. This Z-contrast image presents a typical perovskite structure with four high-intensity Ba atomic columns and one low-intensity Ti atomic column (*19*). The precise atomic stacking matches well with the crystal structure of BTO. Interestingly, we identified the exquisite fringes we observed as equal inclination fringes with the so-called bend contours (*20*). The presence of exquisite bend contours in the hollow areas also proves the single-crystalline nature of the BTO membrane with a uniform thickness and the formation of the buckling state.

We then transferred the BTO membrane onto the Si substrate and tested the electromechanical properties using piezoresponse force microscopy (PFM). We applied V = ±10 V to write an out-of-plane FE domain–switching image (Fig. 1H). We also measured the polarization-voltage loops that the BTO membranes transferred on Pt/Si (fig. S8). We obtained explicit reversible switching of FE domains after positive- and negative-bias poling. We obtained the complete FE switching, as exhibited by the piezoelectric response loops (Fig. 1I).

During the preparation, some of the freestanding BTO membranes were folded (fig. S9). All these folded BTO membranes maintained

[1]Electronic Materials Research Laboratory, Key Laboratory of the Ministry of Education, School of Electronic and Information Engineering, State Key Laboratory for Mechanical Behavior of Materials, International Joint Laboratory for Micro/Nano Manufacture and Measurement Technology, Xi'an Jiaotong University, Xi'an 710049, China. [2]State Key Laboratory for Mechanical Behavior of Materials, Xi'an Jiaotong University, Xi'an 710049, China. [3]Center for Advancing Materials Performance from the Nanoscale (CAMP-Nano) and Hysitron Applied Research Center in China (HARCC), State Key Laboratory for Mechanical Behavior of Materials, Xi'an Jiaotong University, Xi'an 710049, China. [4]National Synchrotron Radiation Laboratory and CAS Key Laboratory of Materials for Energy Conversion, Department of Physics, University of Science and Technology of China, Hefei 230026, China. [5]Shenzhen Key Laboratory of Nanobiomechanics, Shenzhen Institutes of Advanced Technology, Chinese Academy of Sciences, Shenzhen 518055, China. [6]Advanced Research Institute of Multidisciplinary Science, Beijing Institute of Technology, Beijing 100081, China. [7]Department of Chemistry and 4D LABS, Simon Fraser University, Burnaby, BC V5A 1S6, Canada. [8]State Key Lab of New Ceramics and Fine Processing, School of Materials Science and Engineering, Tsinghua University, Beijing 100084, China. [9]Department of Materials Science and Engineering, The Pennsylvania State University, University Park, PA 16802, USA. [10]Department of Nuclear Science and Engineering and Department of Materials Science and Engineering, Massachusetts Institute of Technology, Cambridge, MA 02139, USA.
*These authors contributed equally to this work.
†Corresponding author. Email: mingliu@xjtu.edu.cn (M.L.); ziyaozhou@xjtu.edu.cn (Z.Z.); dingxd@mail.xjtu.edu.cn (X.D.)

integrity and continuity without any cracks. These films behaved like flexible metallic films instead of brittle oxides. Furthermore, we bent the freestanding BTO membranes into several multilayer rolls (fig. S10), which were cut with a focus ion beam (FIB) to prepare cross-sectional transmission electron microscopy (TEM) samples (Fig. 2A). We investigated the structure by choosing four positions with different bending strains labeled with W, X, Y, and Z (Fig. 2A). These areas had different curvatures.

The Y area possessed the strain of up to 3.1% in the BTO roll (Fig. 2A and fig. S11). On the bottom of the BTO rolls, we can distinguish the five BTO layers, and we collected the selected-area electron diffraction pattern at the marked area covering all the layers (fig. S12). We found that all of the layers had the same orientation. The atomic-scale STEM image of the interface between two BTO layers in the Z area indicated that the connection between these BTO layers is by physical adsorption instead of chemical bonding (Fig. 2A). We found a clear Ba atomic column arrangement with a fan-shaped distribution and a continuous strain gradient from the cross-section atomic-scale STEM image of a bent BTO membrane (Fig. 2B). We distinguished two different strained regions, the tensile zone on the top and the compressive strain zone on the bottom. We mapped the accurate strain (ε) distribution directly at the atomic scale by using geometrical phase analysis (*19*, *21*). We calculated strain maps of ε_{xx} and ε_{yy}, which range from −5 to +5% (Fig. 2C).

When an FE membrane is bent, the tensile and compressive regions undergo different local polarization changes at the atomic scale (*22*, *23*). We used HAADF-STEM to image a film with an overlay of the spontaneous polarization direction of BTO (Fig. 2D). We observed multiple polarization orientations in the region where the maximum strain is achieved ε_{max} − 3.1%. Compared with the RSM results, the domain structure was transformed from a single *c*-domain state to a multidomain state by the strain gradient during bending. We showed a more explicit relationship between the lattice distortion and the associated polarization using magnified images from different regions demarcated in Fig. 2, D and E, which is associated with the flexoelectricity (*24*, *25*). We analyzed a series of STEM images with varying conditions of strain to explore the variation of polarization orientation (fig. S13). With the increase of bending stress, the domain state evolved from *c* domains to *a* domains, and we found an intermediate state. The dipoles rotate continuously between the *a* and *c* domains by means of the intermediate state, which does not match the domain characteristics of a tetragonal FE phase. To understand the influence of strain on polarization, we performed atomistic simulations in bent BTO membranes (fig. S14). The simulations that were used had a membrane thickness of 20 nm with the ε_{max} (close to 3.1%) applied. We selected four typical areas to examine the local dipole configuration (Fig. 2F). The polarization orientation was correlated with the strain states in the simulation. Typically, the polarization oriented upward in the compressive strain and tilted downward in the tensile strain while becoming horizontal near the neutral strain region, which was consistent with the experimental observations.

The formation of rolls implies that the freestanding BTO membranes had excellent flexibility, which is a rare feature for functional oxide materials. We manipulated BTO nanobelts using in situ SEM. We fabricated freestanding BTO nanobelts using the FIB and handled them with the nano-manipulator tip in the SEM (fig. S15). We carried out the bending tests on BTO nanobelts with thicknesses of 60 and 120 nm, respectively (Fig. 3). We used one nano-manipulator tip to hold the BTO nanobelt (120 nm), and we used another nano-manipulator tip to push the BTO nanobelt to bend. This process allowed us to bend BTO nanobelts into different curvatures (Fig. 3A). We achieved a maximum strain of ~10% in the BTO nanobelt without any fracture (fig. S16), demonstrating excellent flexibility in this oxide material. We measured the evolution of the elastic properties of a BTO nanobelt (60 nm in thickness) at a bending angle of 40° with different holding durations (Fig. 3B). We were able to instantly recover the strain from this BTO nanobelt. We recovered a large portion of the strain instantaneously even when increasing the bending angle up to 80° (Fig. 3C and movies S1 to S3).

The conventionally brittle BTO has good shape recovery when prepared as nanobelts. The super-elasticity usually is associated with reversible phase transformations like those seen in shape-memory alloys (*2*, *26*). The physical nature of elasticity, in general, is the tolerance that allows large shape deformation and the energy conversion that provides the ability of recovery. We examined the BTO domain architectures under different bending configurations through TEM bright-field imaging (fig. S17), which confirmed that the domain structure is highly dependent on strain state. Additionally, we compared the Raman spectra of the flat and the rolled BTO membranes on glass substrates, which allowed us to exclude structural phase transition during the bending process (fig. S18). In the freestanding BTO membranes, we believe the FE domain switching to be responsible for the observed flexibility and super-elasticity.

We carried out atomistic simulations on the microstructure evolution under mechanical bending in the BTO membranes at 300 K. Figure 4A shows the variation of bending

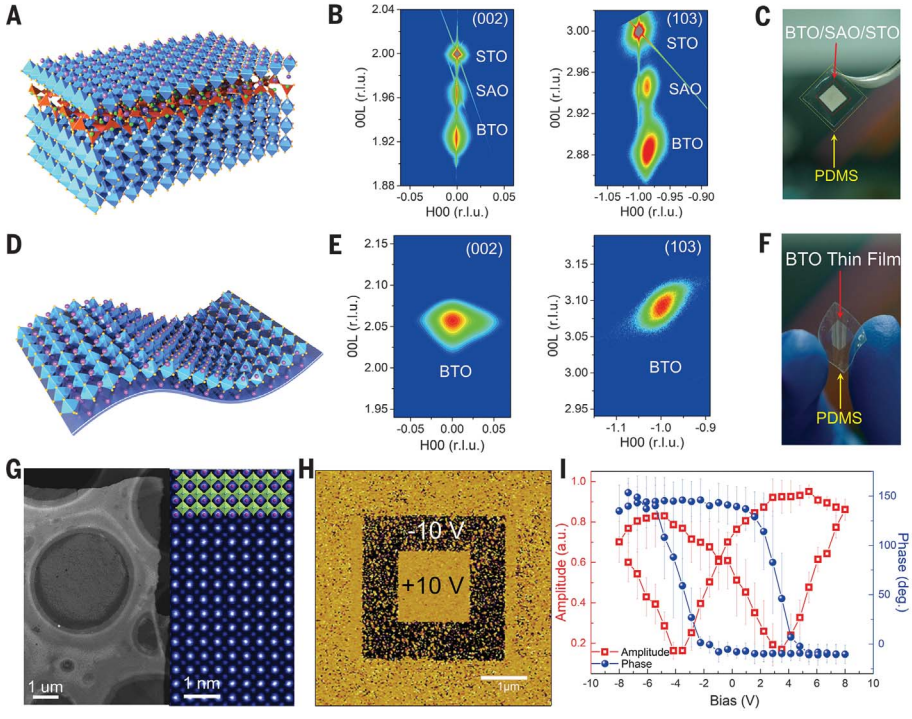

Fig. 1. Synthesis and characterizations of freestanding BTO membranes. Schematics (**A** and **D**), reciprocal space maps (**B** and **E**) around the (002)- and (103)-diffraction condition of STO, and optical photographs (**C** and **F**) of the BTO/SAO/STO heterostructure and flexible BTO membrane, respectively. r.l.u., relative light units. (**G**) Plane-viewed HAADF-STEM images of freestanding BTO membrane supported by a Cu grid with lacey carbon film. (**H**) Out-of-plane PFM phase image of BTO transferred on Pt/Si. (**I**) Piezoelectric response of the BTO membranes transferred on Pt/Si. a.u., arbitrary units.

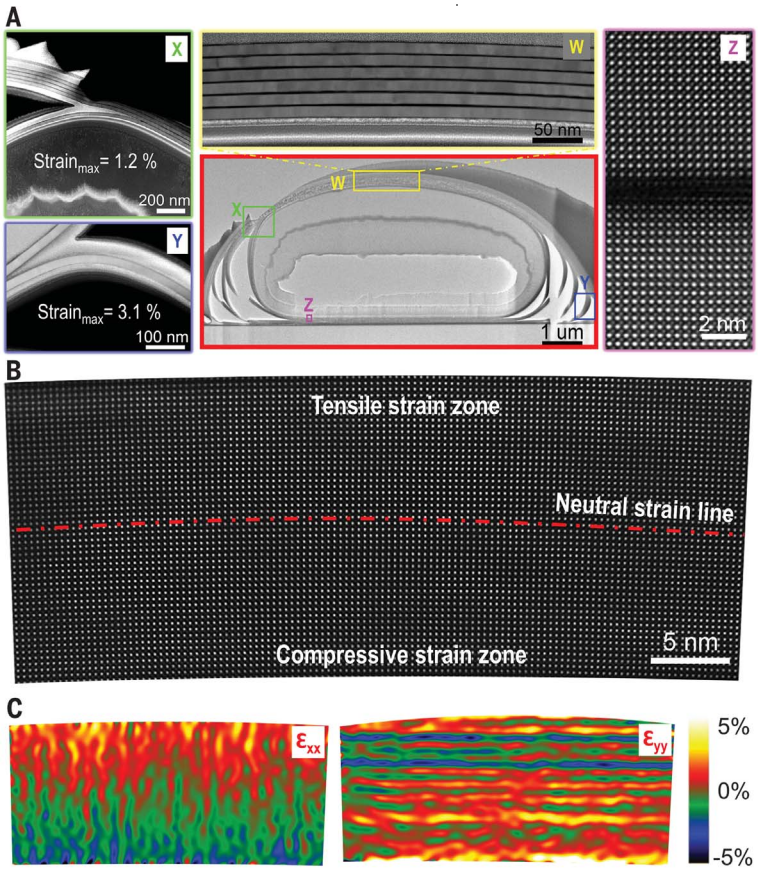

Fig. 2. Atomic-scale spatial distribution of continuous and curved lattice. (**A**) Cross-sectional STEM and TEM images of multilayer BTO roll with magnified images of the different regions, marked by W, X, Y, and Z. W, cross-sectional STEM image of freestanding BTO multilayer; X, the region with strain$_{max}$ ~ 1.2%; Y, the region with strain$_{max}$ ~ 3.1%; Z, the region with near-zero strain. (**B** and **C**) Atomic-scale STEM and geometric phase analysis images of BTO. (**D**) Atomic-scale STEM together with Ti displacement of the region with strain$_{max}$ ~ 3.1%. (**E**) Magnified images of the four regions from (D). Dipole displacements are amplified by a factor of 15 for clarity. (**F**) The dipole configurations in four selected areas of a bent membrane by atomistic simulations. Dipole displacements are amplified by a factor of 50 for clarity.

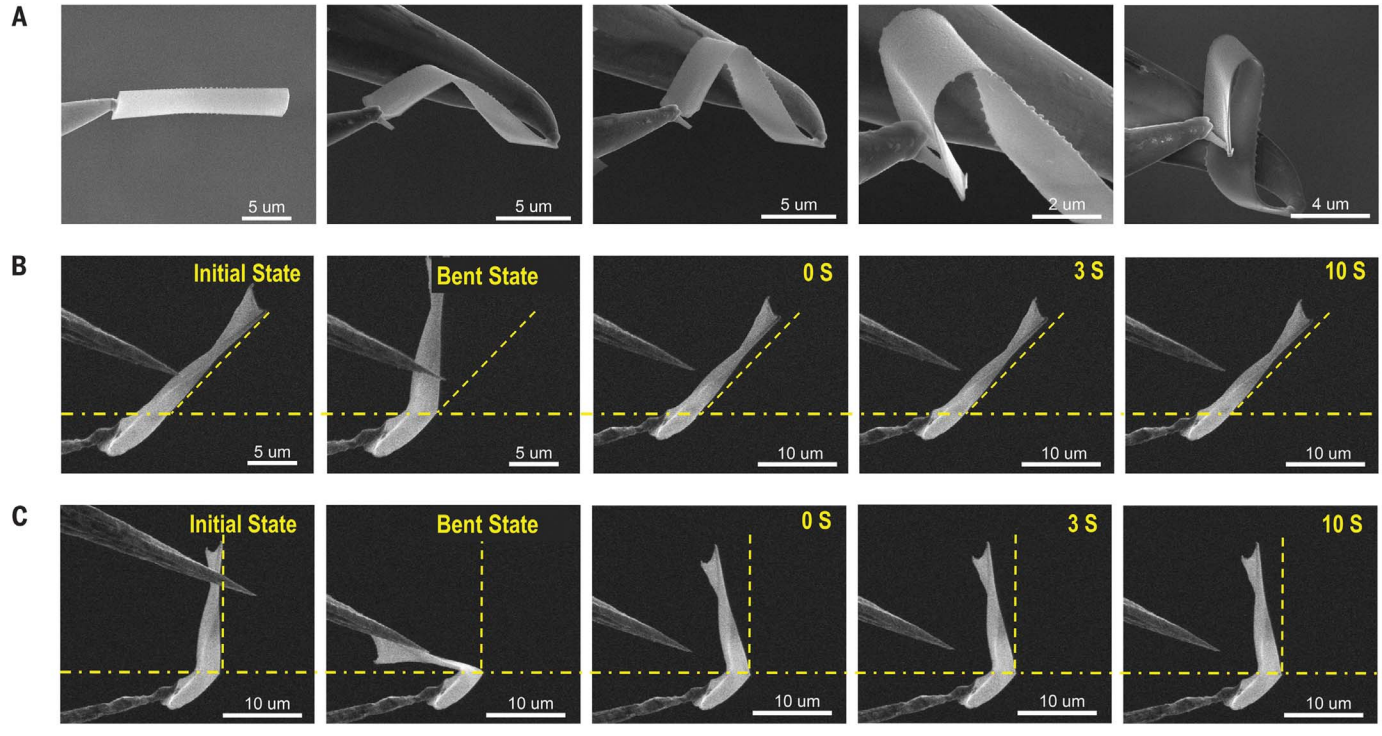

Fig. 3. In situ SEM bending test of BTO nanobelts. (**A**) Series of SEM images with the bending process of a BTO nanobelt (20 μm by 4 μm by 120 nm). (**B** and **C**) SEM images of the recovery process after the different bending states for a BTO nanobelt (20 μm by 4 μm by 60 nm).

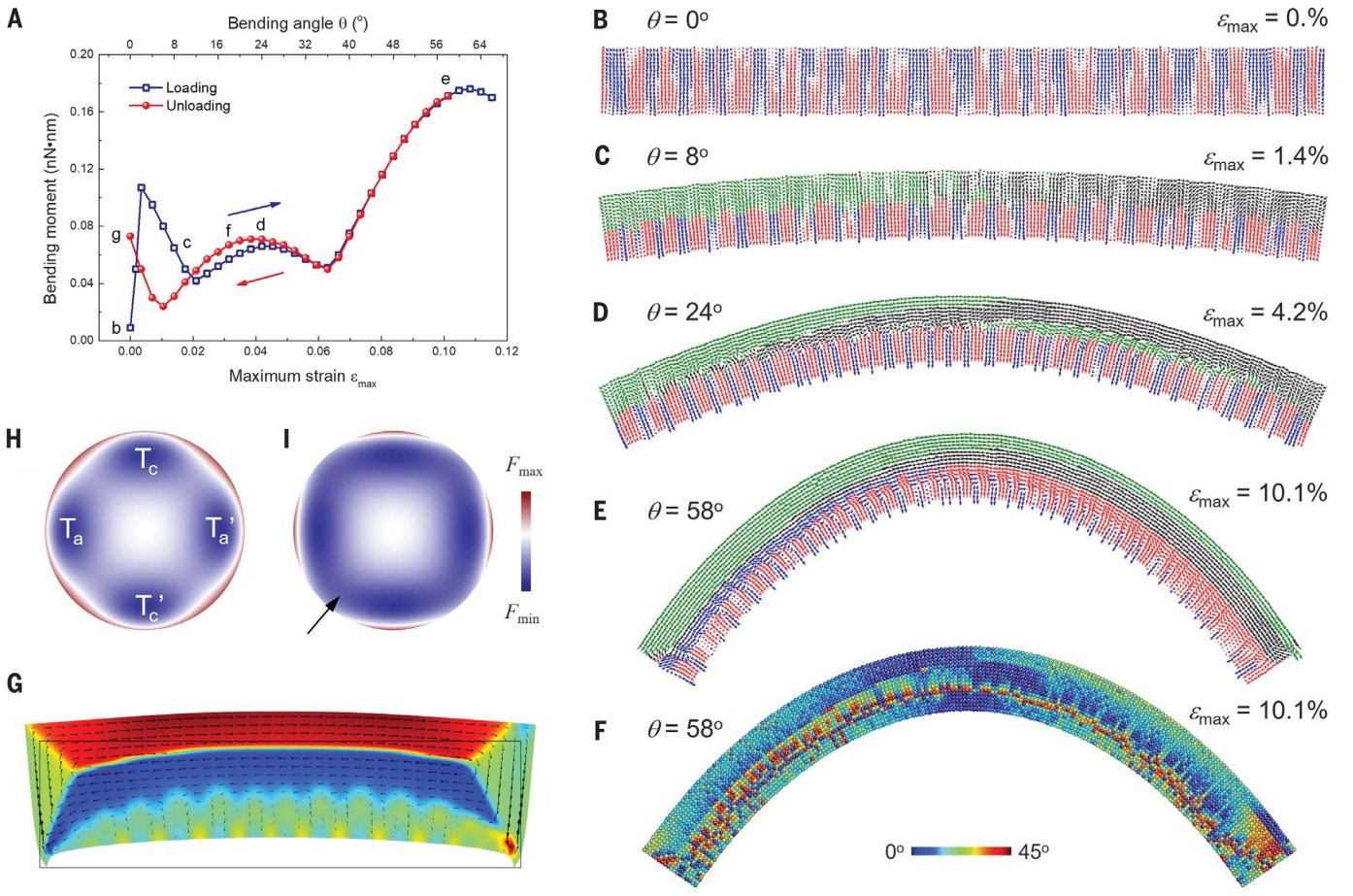

Fig. 4. Shape recovery of the BTO membrane upon bending at 300 K. (**A**) Variation of bending moment with bending angle θ (and maximum strain ε_{max}) upon loading and unloading with sample width of 8 nm. (**B** to **E**) Typical snapshots of dipole configurations at different bending angles. The black and green arrows represent the dipoles with *x* components left and right, respectively, in the tensile region. The red and blue arrows represent the dipoles with *y* components up and down, respectively, in the compressive region. Dipole displacements are amplified by a factor of 50 for clarity. (**F**) Spatial distribution of angle deviation η with respect to the *a* or *c* nanodomain at θ = 58°. η characterizes the deviation of dipole rotation with respect to the *a* or *c* domains by using the parameter $\eta = \pi/4 - |\varphi - (n^*\pi/2 + \pi/4)|$ for $\varphi \in [n^*\pi/2, (n+1)^*\pi/2]$, where φ is the rotation angle of polarization concerning the central axis in each unit cell and *n* runs from 0 to 3. (**G**) Phase-field modeling of the domain structures of the bent BTO membrane. The colors are coded according to the orientations of the domains. (**H** and **I**) Schematic illustration of free energy landscape of bulk BTO and nanomembrane under bending, respectively. (H) T_a (T_a') and T_c (T_c') refer to the tetragonal phases with *a* domains (polarized leftwards and rightwards) and *c* domains (polarized upwards and downwards) in bulk. (I) The energy barrier between *a* and *c* nanodomains drops markedly (indicated by the black arrow), allowing continuous rotation of dipoles in the bent membrane.

moment as a function of bending angle θ (and maximum strain ε_{max}) upon a loading and unloading cycle. The membrane deformed elastically, followed by the plastic flow. Further bending induced a continuous increase of the moment until the final drop, corresponding to the crack nucleation. Upon unloading before fracture, it almost traced back, resulting in a typical super-elastic behavior. The total recoverable strain could reach ~10%, close to our experimental value. We calculated the loss factor of the mechanical hysteresis to be only ~0.02, far below that of ~0.14 in zirconia shape-memory ceramics (*6*) and ~0.2 in Ti–Ni–Cu shape-memory alloys (*27*) at small scale.

To understand the mechanism responsible for such a substantial shape recovery, we examined the evolution of dipole configurations at the atomic scale. Before loading, we identified the lattices as *c* nanodomains with polarization either upward (red arrows) or downward (blue arrows) (Fig. 4B). In the tensile regions, the vertical dipoles began to rotate clockwise or anticlockwise locally at a smaller bending angle (Fig. 4C). Large bending can promote the local nanodomains to merge and transform into *a* nanodomains with polarizations oriented left (black arrows) or right (green arrows) in the tensile region (Fig. 4D). As we applied the considerable bending angle, one oriented *a* nanodomain grew to cover the whole free surface, forming a 180° domain boundary with a few steps (Fig. 4E). The polarizations prefer to be upward in the compressive region such that the 180° domain switching occurs from downward to upward in some local areas. Because the twin wall energy is usually very small in FEs (*28*–*31*), the energy cost of forming such high-density nanodomains is not that high. The dipoles almost switch back upon unloading (movies S4 and S5). However, the *a* domains cannot revert to *c* domains completely in the tensile region (fig. S19). Thus, the membrane cannot achieve a full shape recovery, because of the irreversible transformation of domain patterns locally.

We know the bulk BTO is brittle under a minimal strain. The fracture is usually originated from the initiation of crack near the internal flaw or along the grain boundaries. Two reasons might account for the flexibility in our BTO membranes. First, the flaw density is markedly reduced in such a smaller sample in comparison with its bulk counterpart. The paucity of flaw would avoid stress concentration and suppress the nucleation of crack in the interior of the sample. Unlike the bulk where

180° and 90° domains usually form, we observed that dipoles rotate continuously in a transition zone connecting *a* and *c* domains (Fig. 4F and fig. S20), similar to the rotation of polarizations across the 180° twin walls observed in the tetragonal $PbZr_{0.2}Ti_{0.8}O_3$ films experimentally (*32*, *33*). The flexoelectric effect is the primary driving force for the polarization rotation in *a* and *c* nanodomains far away from the neutral strain line (*34*) but only contributes partially in the transition zone (supplementary materials). The formation of such a continuous transition zone could largely eliminate the mismatch stress in the coexisting *c* and *a* nanodomains at high strain, avoiding the mechanical failure by the sharp domain switching. This transition zone exists in samples with a thickness ranging from 6.4 to 11.2 nm (fig. S21). In addition, Fig. 4G shows the domain structure of the bent BTO membrane under a high strain, obtained from phase-field simulation. We observed a similar dipole configuration, consistent with the experimental and the atomistic simulation results.

We emphasized that the continuous transition occurs when the size reduces to the nanoscale (*35*–*37*). According to the phenomenological Landau theory (*38*, *39*), four minima in the energy landscape exist in the bulk stress-free state, corresponding to two oriented *a* domains and *c* domains separately (Fig. 4H). Following the smaller-is-stronger trend (fig. S21), a high stress could be reached at nanoscale, and such high stress could modify the landscape markedly. Consequently, the energy barrier between *a* and *c* domains would be reduced, generating the metastable states in which dipoles are able to stay with some deviations from *a* or *c* domains (Fig. 4I). This metastable state in the transition zone could easily revert to the *a*- or *c*-domain state when removing the load. This would account for why we might observe shape recoverability at nanoscale rather than in bulk.

Combined with the intrinsic piezoelectricity and ferroelectricity and the flexoelectric effects (fig. S22 and S23) integrated by lattice and strain, especially in a two-dimensional structure, the reported super-elasticity in the BTO membranes is expected to provide more degrees of freedom for a wide range of applications in nanotechnology. Additionally, the flexible FE membranes can also serve as a viable platform to explore strain-triggered correlated phenomena, such as functionality enhancement, FE domain engineering, and phase transitions, in future research.

REFERENCES AND NOTES

1. T. B. M. C. Barret, *Structure of Metals*, (Pergamon, Oxford, UK, 1992).
2. J. F. Gómez-Cortés *et al*., *Nat. Nanotechnol.* **12**, 790–796 (2017).
3. G. Cheng *et al*., *Nat. Nanotechnol.* **10**, 687–691 (2015).
4. S. L. Wang, Z. W. Shan, H. Huang, *Adv. Sci.* **4**, 24 (2017).
5. J. Cao *et al*., *Nat. Nanotechnol.* **4**, 732–737 (2009).
6. A. Lai, Z. Du, C. L. Gan, C. A. Schuh, *Science* **341**, 1505–1508 (2013).
7. T. Leydecker *et al*., *Nat. Nanotechnol.* **11**, 769–775 (2016).
8. F. R. Fan, W. Tang, Z. L. Wang, *Adv. Mater.* **28**, 4283–4305 (2016).
9. Q. Zheng, B. J. Shi, Z. Li, Z. L. Wang, *Adv. Sci.* **4**, 23 (2017).
10. D. Lu *et al*., *Nat. Mater.* **15**, 1255–1260 (2016).
11. S. R. Bakaul *et al*., *Nat. Commun.* **7**, 10547 (2016).
12. L. Chang, L. You, J. L. Wang, *Jpn. J. Appl. Phys.* **57**, 7 (2018).
13. D. Ji *et al*., *Nature* **570**, 87–90 (2019).
14. Y. Qi *et al*., *Nano Lett.* **10**, 524–528 (2010).
15. Z. G. Zuo *et al*., *J. Phys. D Appl. Phys.* **45**, 5 (2012).
16. L. Hong *et al*., *Phys. Rev. B Condens. Matter Mater. Phys.* **77**, 7 (2008).
17. S. Sahoo *et al*., *Phys. Rev. B Condens. Matter Mater. Phys.* **76**, 092108 (2007).
18. Materials and methods are available as supplementary materials.
19. C. Dubourdieu *et al*., *Nat. Nanotechnol.* **8**, 748–754 (2013).
20. E. Spiecker, *Ultramicroscopy* **92**, 111–132 (2002).
21. J. L. Rouvière, E. Sarigiannidou, *Ultramicroscopy* **106**, 1–17 (2005).
22. I. Stolichnov *et al*., *Nano Lett.* **15**, 8049–8055 (2015).
23. Z. B. Chen *et al*., *Phys. Rev. Lett.* **118**, 7 (2017).
24. T. D. Nguyen, S. Mao, Y. W. Yeh, P. K. Purohit, M. C. McAlpine, *Adv. Mater.* **25**, 946–974 (2013).
25. W. J. Chen, Y. Zheng, X. Feng, B. Wang, *J. Mech. Phys. Solids* **79**, 108–133 (2015).
26. Y. Tanaka *et al*., *Science* **327**, 1488–1490 (2010).
27. J. San Juan, M. L. Nó, C. A. Schuh, *Nat. Nanotechnol.* **4**, 415–419 (2009).
28. D. D. Viehland, E. K. H. Salje, *Adv. Phys.* **63**, 267–326 (2014).
29. Y. M. Jin, Y. U. Wang, A. G. Khachaturyan, J. F. Li, D. Viehland, *J. Appl. Phys.* **94**, 3629–3640 (2003).
30. D. Viehland, *J. Appl. Phys.* **88**, 4794–4806 (2000).
31. Y. M. Jin, Y. U. Wang, A. G. Khachaturyan, J. F. Li, D. Viehland, *Phys. Rev. Lett.* **91**, 4 (2003).
32. G. De Luca *et al*., *Adv. Mater.* **29**, 1605145 (2017).
33. S. Cherifi-Hertel *et al*., *Nat. Commun.* **8**, 15768 (2017).
34. G. Catalan *et al*., *Nat. Mater.* **10**, 963–967 (2011).
35. D. A. Cogswell, M. Z. Bazant, *Electrochem. Commun.* **95**, 33–37 (2018).
36. Z. Zhang *et al*., *Phys. Rev. Lett.* **111**, 5 (2013).
37. D. A. Cogswell, M. Z. Bazant, *Nano Lett.* **13**, 3036–3041 (2013).
38. Y. J. Gu *et al*., *Phys. Rev. B Condens. Matter Mater. Phys.* **89**, 11 (2014).
39. Y. L. Li, L. Q. Chen, *Appl. Phys. Lett.* **88**, 3 (2006).

ACKNOWLEDGMENTS

We thank D. Wang, H. Nan, and L. Lu (Xi'an Jiaotong University) for developing the APPSA software for locating the atomic positions and TEM sample preparation and R. Ramesh (University of California, Berkeley), X. Wang, X. Zhuang (Tongji University), and C. Guo (Beijing Institute of Technology) for fruitful discussions. **Funding:** We acknowledge the support from the National Key R&D Program of China (grant 2018YFB 0407601), the Natural Science Foundation of China (grants 11534015, 51602244, 51802248, 11574246, 51931004, 51621603, 51788104, 11374010, 11675179), the National 111 Project of China (grant B14040), the National Key R&D program (2016YFA0300102), National Key Research and Development Program of China (grant 2016YFA0201001 to J.Y., T.J., and J.L.), and the Natural Sciences and Engineering Research Council of Canada (grant 203773 to Z.-G.Y.). **Author contributions:** M.L. and Z.Z. designed and supervised the project. G.D. and M.Y. fabricated the films. G.D. conducted STEM and TEM experiments and the data analysis. S.L., J.S., Ju.L., and X.D. carried out the atomistic simulations. Y.-Q.Z. performed the in situ SEM experiments. X.H. and Z.L. conducted the RSM tests. J.Y., T.J., and Ji.L. conducted the PFM tests. H.H. and L.-Q.C. performed the phase-field simulations. B.P., Z.H., W.R., Z.-G.Y., and C.-W.N. conducted the ferroelectric measurements. G.D., Z.Z., S.L., and M.L. wrote the first draft of the manuscript. All authors contributed to the discussion of the results and the revision of the manuscript. **Competing interests:** The authors declare no competing interests. **Data and materials availability:** All data are available in the manuscript or the supplementary materials.

SUPPLEMENTARY MATERIALS

science.sciencemag.org/content/366/6464/475/suppl/DC1
Materials and Methods
Supplementary Text
Figs. S1 to S23
Movies S1 to S5
References (*40*–*51*)

13 July 2019; accepted 30 September 2019
10.1126/science.aay7221

Super-elastic ferroelectric single-crystal membrane with continuous electric dipole rotation

Guohua Dong, Suzhi Li, Mouteng Yao, Ziyao Zhou, Yong-Qiang Zhang, Xu Han, Zhenlin Luo, Junxiang Yao, Bin Peng, Zhongqiang Hu, Houbing Huang, Tingting Jia, Jiangyu Li, Wei Ren, Zuo-Guang Ye, Xiangdong Ding, Jun Sun, Ce-Wen Nan, Long-Qing Chen, Ju Li and Ming Liu

Science **366** (6464), 475-479.
DOI: 10.1126/science.aay7221

Flexible ferroelectrics

High-quality ferroelectric materials, which polarize in response to an electric field, are usually oxides that crack when bent. Dong *et al.* found that high-quality membranes of barium titanate are surprisingly flexible and super-elastic. These films accommodate large strains through dynamic evolution of nanodomains during deformation. This discovery is important for developing more robust flexible devices.

Science, this issue p. 475

Supplementary Materials for

Super-elastic ferroelectric single-crystal membrane with continuous electric dipole rotation

Guohua Dong*, Suzhi Li*, Mouteng Yao*, Ziyao Zhou†, Yong-Qiang Zhang, Xu Han, Zhenlin Luo, Junxiang Yao, Bin Peng, Zhongqiang Hu, Houbing Huang, Tingting Jia, Jiangyu Li, Wei Ren, Zuo-Guang Ye, Xiangdong Ding†, Jun Sun, Ce-Wen Nan, Long-Qing Chen, Ju Li, Ming Liu†

*These authors contributed equally to this work.
†Corresponding author. Email: mingliu@xjtu.edu.cn (M.L.); ziyaozhou@xjtu.edu.cn (Z.Z.); dingxd@mail.xjtu.edu.cn (X.D.)

Published 25 October 2019, *Science* **366**, 475 (2019)
DOI: 10.1126/science.aay7221

This PDF file includes:

Other Supplementary Material for this manuscript includes the following:
(available at science.sciencemag.org/content/366/6464/475/suppl/DC1)

Materials and Methods

Target Preparation and Thin Film Deposition

$BaTiO_3$ (BTO) target was prepared by mixing $BaCO_3$ and TiO_2 powders in the conventional solid-state way, followed by a sintering process at 1200 °C for 3 hours in a high-temperature furnace. $Sr_3Al_2O_6$ (SAO) target was prepared by mixing $SrCO_3$ and Al_2O_3 powders with the same method. These targets were used to fabricate the epitaxial films, which were then deposited on the $SrTiO_3$ (STO) substrates through a pulsed laser deposition (PLD) system with a KrF excimer laser of 248 nm wavelength. The base pressure was below 1×10^{-6} Torr, and sample-target distance was 5.0 cm. During the deposition, the energy density of the laser beam focused onto the targets was adjusted to be 1.8 J/cm^2 and 2.0 J/cm^2 for BTO and SAO while the oxygen partial pressure was maintained at 100 mTorr and 150 mTorr, respectively. The laser pulse rate was 3 Hz, and the substrate temperature was held at 750 °C.

Details of Single Crystal Membrane Peeling and Transferring Method:

The SAO layer was completely removed in de-ionized water at room temperature. Before the SAO layer was removed, the protecting layers such as polydimethylsiloxane (PDMS), PMMA or other supporting layers should be coated on the BTO membrane to ensure the integrity of the membranes. The membranes were immersed in the de-ionized water to dissolve the sacrificial SAO layer. Then, the large-scale freestanding membrane can be transferred onto silicon, glass, flexible PET/Mica substrates, and so on.

Structural and Electrical Characterizations:

The crystal structure of the membranes was investigated by using high-resolution synchrotron x-ray, at 14B Beamline of the Shanghai Synchrotron Radiation Facility (SSRF). High-resolution X-ray diffraction measurements (Theta-2theta) was conducted by a PANalytical Empyrean diffractometer. In-situ SEM bending test on BTO nanobelts was conducted by FIB (Helios NanoLab DualBeam) with Kleindiek mechanical manipulators. BTO nanobelts were fabricated from the large area freestanding membrane using FIB (Ga^+ sources, low ion current). Atomic-resolution high-angle annular dark-field (HAADF) and annular bright-field (ABF) images were obtained through a JEM ARM200F microscope with Cs-corrected STEM operated at 200kV. The ferroelectric domains and polarization reversal behaviors were characterized by piezoresponse force microscopy (PFM, Asylum Cypher). The polarization-electric field loops were displayed using an aixACCT ferroelectric test system (TF-Analyser 2000, aixACCT, Germany) at a frequency of 1 kHz.

Atomistic Simulations

We used the core-shell model (*40, 41*) to describe the interatomic interactions of $BaTiO_3$. Each atom consists of two coupled charged particles, i.e., the core with a positive charge and the shell with a negative charge. The total potential energy of the system contains three parts, i.e., the anharmonic spring energy between the core and shell, the short-range interaction between shells of different atoms and the long-range Coulombic interaction between the core and shell of different atoms (*42*). The basic properties predicted by this potential show an excellent agreement with those obtained by the DFT calculations (*40*), such as temperature-induced phase transition and polarization, etc.

The $BaTiO_3$ membrane with a tetragonal structure was first constructed with the orientations of *x*-[100], *y*-[010] and *z*-[001] at 300 K. The membrane was found to be single crystalline experimentally. To reduce the high computing cost for calculating long-range interactions, we have created a quasi-2D model with only one lattice unit in *z* direction because the additional layers will not change the microstructures significantly. The aspect ratio was 10. The periodic boundary condition was applied along the *z* direction, and free boundaries were applied in the other two directions.

To perform bending deformation, several atomic layers at both ends of the membrane were fixed rigidly as the loading grip. The bending was achieved by tilting the rigid loading ends against each other. The tilt was performed at a prescribed increment of $\Delta\theta$ = 2°, followed by relaxation at the present strain for 100 ps. The bending moment was evaluated by averaging over the last 50 ps. The bending moment was calculated by integrating the moments of all atomic sites in the cross-sectional area as $\int \sigma_n l dS$, where σ_n is the normal stress for each atomic site in the loading grid, *l* is the distance from the atomic site to the neutral line and *S* is the cross-sectional area of the loading grid. Unloading was performed in a similar way by reducing the tilt angle. The polarization density was calculated as $P = qs/V$, where *q* is the charge of Ti, *s* is the total net displacement in the whole system, and *V* is the system volume. Here $q = 3.072\times10^{-19}$ C in the current core-shell model. The simulations were performed at 300 K using a Nosé-Hoover thermostat (*43*) with the LAMMPS (*44*). The atomic configurations were displayed using AtomEye (*45*).

Phase-Field Modelling

We investigate ferroelectric polarization switching by using phase-field modelling, BTO membrane bending was simulated by solving the time-dependent Ginzburg-Landau equation,

$$\frac{\partial \boldsymbol{P_i}(\boldsymbol{r},t)}{\partial t} = -L\frac{\delta F}{\delta \boldsymbol{P_i}(\boldsymbol{r},t)}, i = 1,2,3 \qquad (1)$$

where $\boldsymbol{P_i}(\boldsymbol{r},t)$ is polarization, L is a kinetic coefficient that is related to the domain wall mobility, and F is the total free energy that includes the contributions from Landau energy, elastic energy, electric energy and gradient energy.

$$F = \iiint \left(f_{Land} + f_{elas} + f_{elec} + f_{grad}\right)dV \qquad (2)$$

The Landau energy density f_{Land} is described by a Landau-Devonshire polynomial and detailed expression can be found in the literature (*46*). The elastic energy density is described using the expression,

$$f_{elas} = C_{ijkl}\left(\varepsilon_{ij} - \varepsilon_{ij}^0\right)\left(\varepsilon_{kl} - \varepsilon_{kl}^0\right) \qquad (3)$$

where C_{ijkl} is the elastic stiffness tensor, ε_{ij} and ε_{ij}^0 are the total local strain, and the spontaneous strain, respectively. The electric energy density f_{elec} is given by,

$$f_{elec} = -\frac{1}{2}\varepsilon_0\kappa_{ij}E_iE_j - E_iP_i \qquad (4)$$

where E_i is the electric field component, which includes both the applied electric field and the depolarization field, ε_0 and κ_{ij} are the vaccum permittivity and dielectric constant, respectively. The gradient energy density in an anisotropic system can be calculated by,

$$f_{grad} = \frac{1}{2}\gamma_{ijkl}P_{i,j}P_{k,l} \qquad (5)$$

where γ_{ijkl} is the gradient energy coefficient, and $P_{i,j} = \frac{\partial P_i}{\partial x_j}$.

In this work, the ferroelectric membrane of BTO is discretized at grid size 80 Δx×1 Δx×20 Δx, with short-circuit boundary conditions applied along the boundaries *z* direction. Δx is set to 1 nm, and the temperature is taken to be 300 K.

Supplementary Text

The TEM angular bright-field (ABF) imaging under various bending conditions

TEM angular bright-field (ABF) imaging (Fig. S17) with strong phase contrast has been employed to reveal the domain structures under different bending angles in ferroelectrics, since domains with different polarization vectors present distinct phase contrasts. In the initially-flat state, the domain width is relatively large, 40~50 nm, and the domain boundary is relatively sharp and almost along an out-of-plane direction (180^o boundary) from the bottom to the top, i.e. *c* domains, as shown in Fig. S17. With the increase of the bending angle, the domain size decreases, e.g., 30~40 nm for the state with a bending angle of ~ 10^o (Fig. S17B), and 20~30 nm for the state with a bending angle of ~ 30^o (Fig. S17C), and the domain boundaries become blurrier and deviate from the out-of-plane direction, i.e., changing to *a* domains or to the coexisting states of *a*- and *c*- domains (*47*). Moreover, at the bottom part (compressed region) of the bent film, the domain state shows a contrast different from that of the top part, with roughly in-plane boundary between them, as shown in Fig. S17D, which confirms that the domain states are different between the top (tensile) and the bottom (compressive) regions of the bent film.

The Raman spectra of the BTO membrane and roll on glass substrates

Raman spectra of the flat BTO membrane and roll on glass substrates were measured, as shown in Fig. S18. The most distinct phonon lines are observed in the flat BTO membrane at about 190, 233, 280, and 522 cm^{-1}, corresponding to the LO1, TO1, TO2, and TO3 modes of A1 symmetry, respectively, which are assigned to the tetragonal phase of BTO. The intensity and frequency of the Raman peaks in the BTO roll at 300 K are nearly the same as those of the flat BTO membrane. The Raman spectroscopy results allow us to exclude the structural phase transition in the bent BTO membranes and its possible effects. Therefore, we can conclude with confidence that the high flexibility of BTO freestanding membrane can be primarily attributed to domain switching, rather than to any structural phase transition.

The dipole configurations of 8 nm-width BTO membrane during bending deformation

To study the super-elasticity of the membranes by atomistic simulations, we performed the bending deformation on the 8 nm-width membranes upon loading/unloading, as illustrated in the manuscript. As show in Fig. S19 show that the typical snapshots of atomic configurations at different bending angles upon the first loading/unloading cycle. The colors represent the dipole rotation angle φ concerning the central axis of the unit lattice.

As we mentioned in the manuscript, there formed a transition zone that could significantly release the mismatch stress in differently oriented domains. We use the parameter η to illustrate such a transition zone. Fig. S20 shows the distribution of η different bending angles upon loading/unloading.

The size effect of the super-elasticity of bending behavior

We finally studied the size effect on the deformation behavior. We varied the thickness of the membranes ranging from 6.4 nm to 11.2 nm while keeping the aspect ratio to be 10. To compare the bending in samples with different sizes, we calculated the effective stress as a bending moment divided by thickness cubed. Fig. S21A shows the dependence of effective stress as the function of bending angles in different samples. There is a noticeable size effect that the smaller size has a higher strength. Moreover, all the samples could sustain a large bending deformation at a bending angle exceeding 60^o. The transition zone exists in all samples and plays an important role in the complement of super-elastic behavior, as shown in Fig. S21(B-E).

The flexoelectric effect of BTO membrane

The large bending deformation corresponds to a more significant strain gradient as $\partial \varepsilon_{xx}/\partial y = 2\theta/L$, where θ is the tilting angle and L is the length of the membrane. The coupling between polarization and strain gradient could induce the flexoelectric effect as $P_y = \mu_{xxyy}\partial \varepsilon_{xx}/\partial y$, where μ_{xxyy} (or μ_{12}) is the flexoelectric coefficient. Fig. S22 shows that the polarization density and strain gradient follow an almost linear relationship upon loading and unloading although there is a small deviation at the early stage of loading, which leads to a typical flexoelectric effect. The flexoelectric coefficient is determined to be around 0.9 nC/m. There are limited experimental data on measuring the perovskite ceramics. For example, μ_{12} is 7 nC/m in $SrTiO_3$ experimentally (*48*). However, the measured experimental coefficient is ~ 50 μC/m for BTO system (*49*), several orders of magnitude of discrepancy with that by DFT calculations (~ nC/m) (*50*). Early studies have shown the flexoelectric effect could be enhanced at nanoscale (*41, 51*). The

functional properties, together with the good recovery in cyclic loading, imply the potential applications as smart nano-devices in BTO.

The influence of the flexoelectric field on the polarization rotation

The coupling between strain gradient and polarization could generate a flexoelectric force, which could partially contribute to the dipole rotation, as proposed by Catalan et al. (*32*). We found that, in the areas far away from neutral strain line, i.e. *a*-domains in tensile region and *c*-domains in compressive region, the polarization rotation is primarily driven by the flexoelectric field. However, near the neutral strain line, we observed a transition zone connecting *a*- and *c*-domains where dipoles could rotate continuously. In this transition zone, the mechanically-induced energy landscape change takes a dominant role on the polarization rotation rather than flexoelectric field. In the following we present the relevant analysis in details.

Our simulation results show that polarizations undergo certain rotation in the *a*- and *c*-domains far away from the neutral strain line, as illustrated in Fig. S20. At θ = 58°, the rotation angle is around 14° (cyan colors near the surfaces). To explore the flexoelectric effect on polarization reorientation, we estimated the flexoelectric force in our bent samples. The coupling of strain gradient along the *y* direction ($\partial \varepsilon_{xx}/\partial y$) and polarization could produce a horizontal flexoelectric force $\mu_{12}\partial \varepsilon_{xx}/\partial y$, where μ_{12} (= 0.9 nC/m) is the flexoelectric coefficient. At θ = 58°, P_{flexo} is estimated to be ~ 0.023 C/m^2. The ferroelectric polarization of BTO in the tetragonal phase is 0.15 C/m^2. The rotation angle in *a*- or *c*-domain is estimated to be ~10°, close to what we observed in simulations.

There, it can be confirmed that the polarization reorientation is governed by the flexoelectric field in the *a*- and *c*-domains far away from the neutral strain line.

On the other hand, near the neutral strain line, our simulation indicates a transition zone appears, which connects *a*- and *c*-domains where dipoles could rotate continuously (Fig. S20). The rotation angle is rather large, far beyond the value estimated by the flexoelectric field. As we discussed in the manuscript, this continuous rotation primarily results from the reduction of the activation barrier of domain switching under the external stress, though the flexoelectric force still takes partial contribution to the polarization rotation. Indeed, the formation of this transition zone takes a key role on achieving the shape recovery ability of our BTO membranes.

Shape recovery upon cyclic bending

To examine the shape recovery ability of membranes in cyclic loading, starting from the final state of 8nm-width membrane, we carried out the second set of loading and unloading deformation. Fig. S23A shows the variation of bending moment as the function of maximum strain (and bending angle). We find that it can still exhibit the full shape recovery behavior during the second bending deformation. Fig. S23B-F shows the typical configurations at different bending angles. The achievement of shape recovery is still based on the domain switching and domain boundary movement. Fig. S23G shows the variation of polarization density with the strain gradient, which indicates the excellent performance of flexoelectricity.

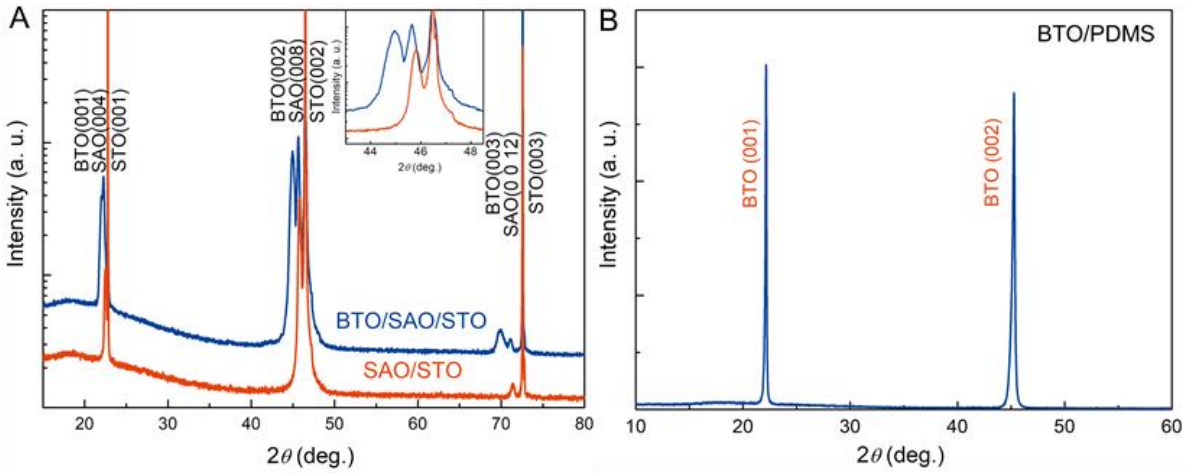

Fig. S1.

Epitaxial growth of BTO/SAO heterostructure. (**A**) The XRD patterns of BTO/SAO/STO and SAO/STO films. (**B**) XRD pattern of BTO/PDMS. The θ-2θ pattern confirms the c-axis oriented BTO/SAO heterostructure. Separated from the STO substrates, the BTO membranes were transferred on the flexible PDMS film. XRD pattern of BTO/PDMS reveals the single crystal characteristics.

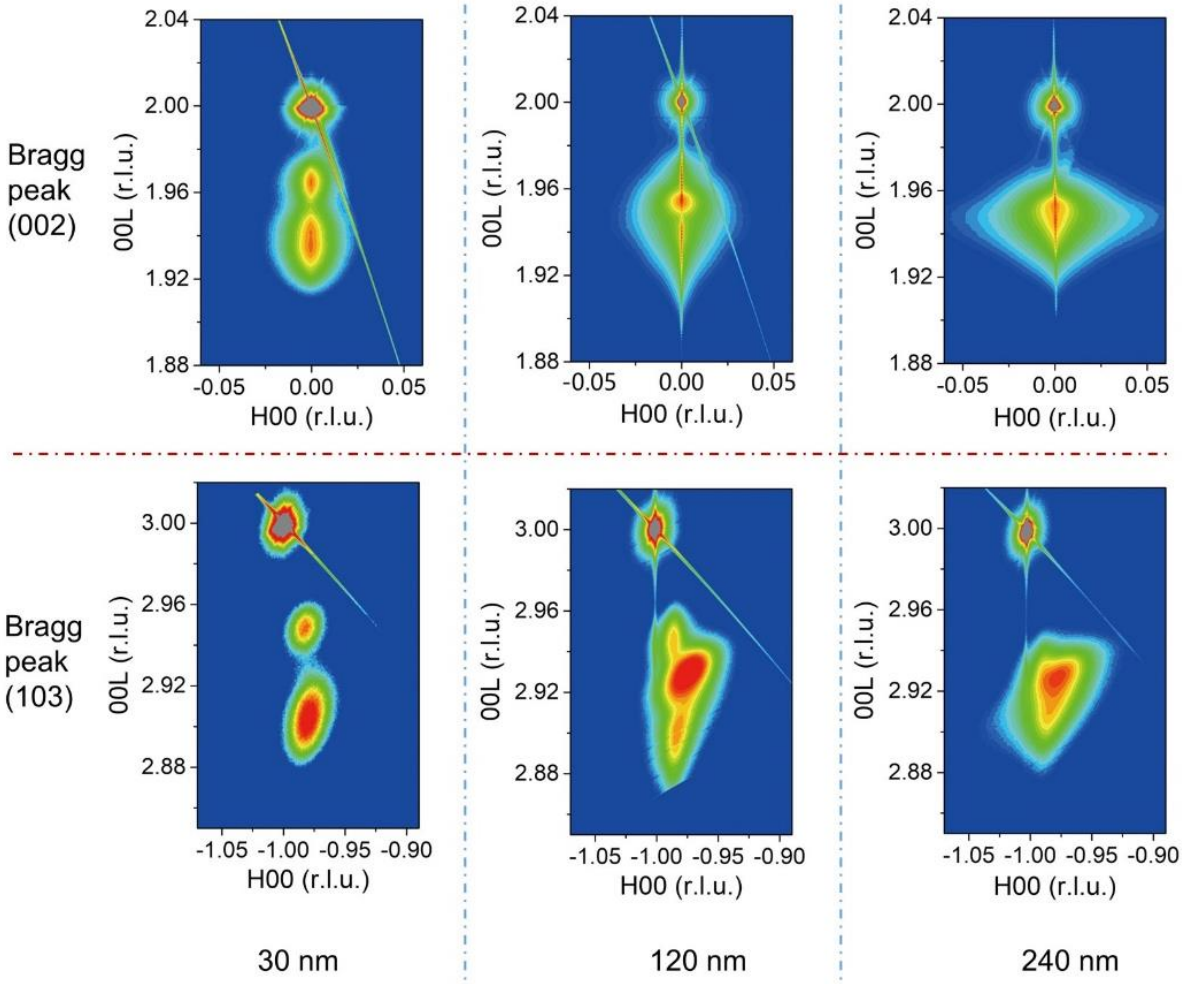

Fig. S2.

Crystal structure of BTO/SAO heterostructure. Reciprocal space map of BTO/SAO/STO heterostructure around the STO Bragg peaks (002) and (103). Interestingly, the BTO films were fully strained by the SAO buffer and STO substrate for thickness of 30 and 60 nm with one symmetric spot. However, the RSM around the (103) Bragg reflection for a 120-nm-thick BTO film was split into two spots, indicating the coexistence of *a*- and *c*-domains.

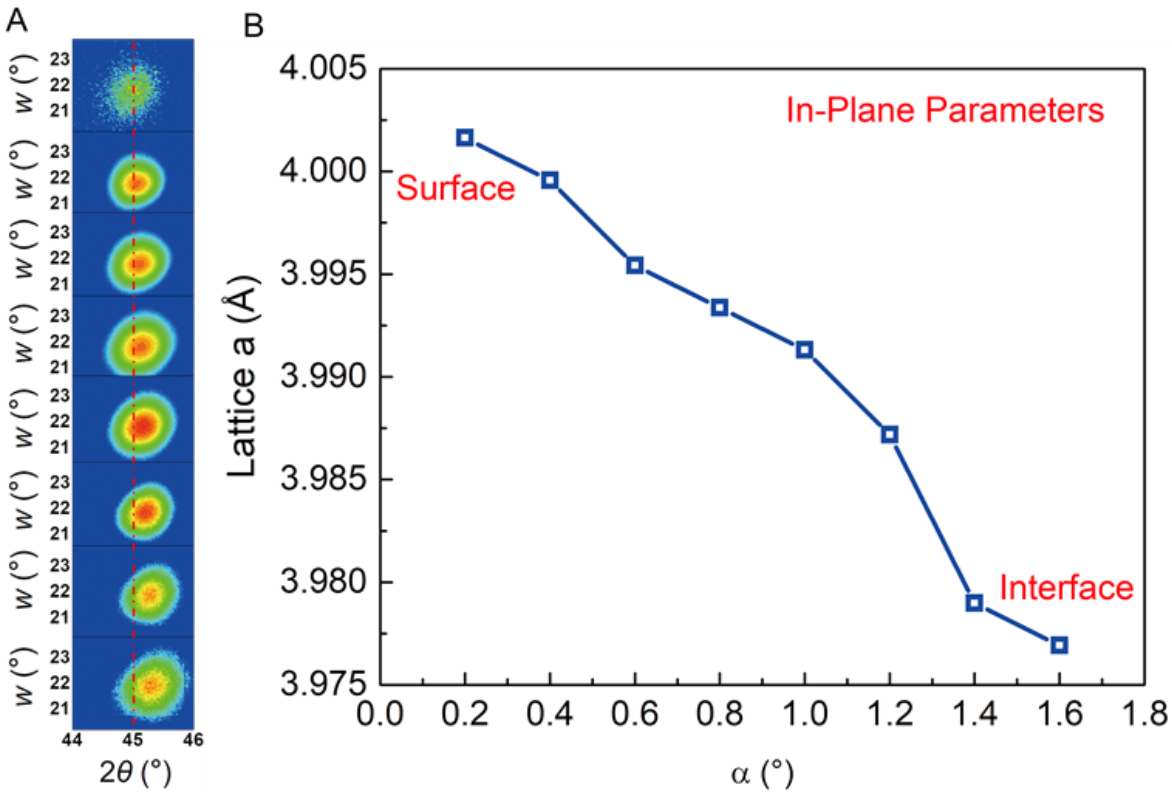

Fig. S3.

In-plane parameters measurements. (A) The GIXRD of 120-nm-thick BTO film. **(B)** With grazing incident angle α dependent in-plane parameters measurements. Strain relaxation was vividly presented in the results.

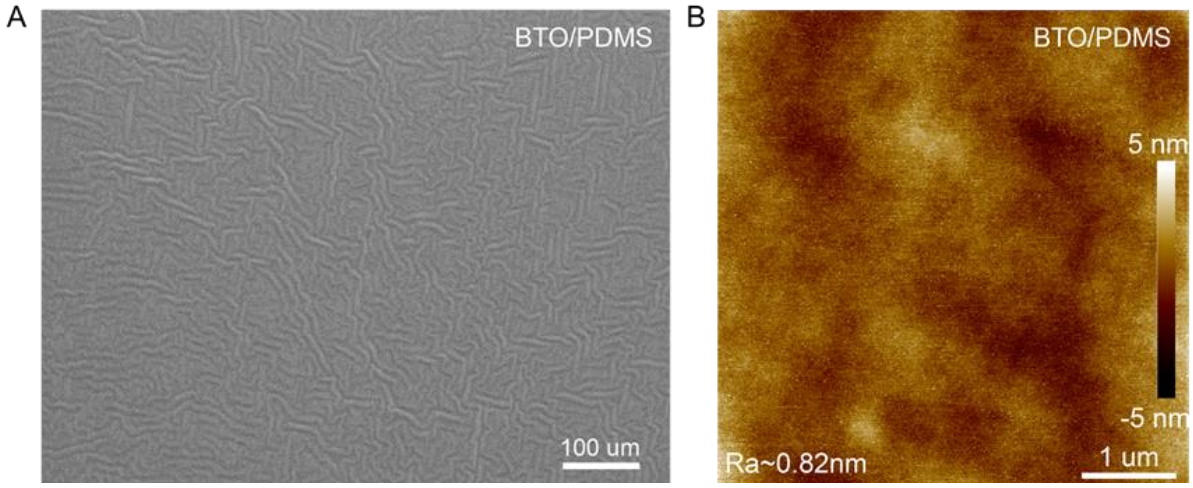

Fig. S4.

Morphology of BTO/PDMS. (A) SEM image of BTO/PDMS. **(B)** AFM image of BTO/PDMS

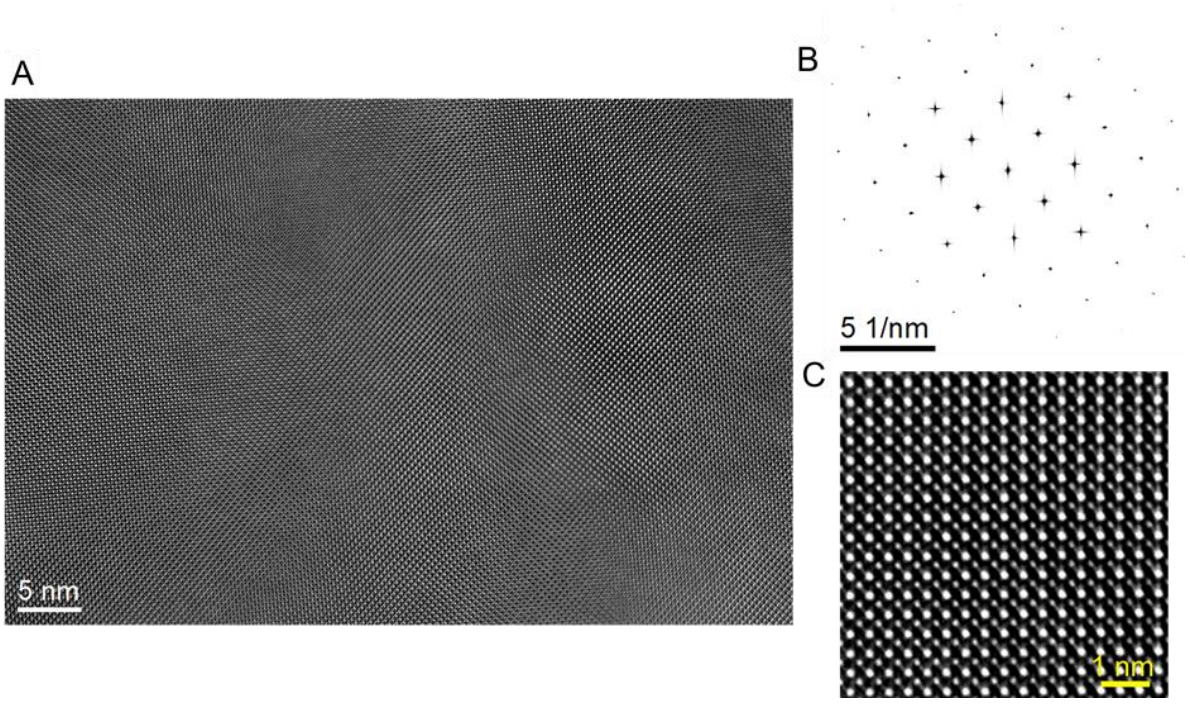

Fig. S5.

Microstructure of freestanding BTO membrane. (A) The high resolution TEM images of freestanding BTO membrane. **(B)** FFT image of the region from HRTEM image. **(C)** The magnified HRTEM image.

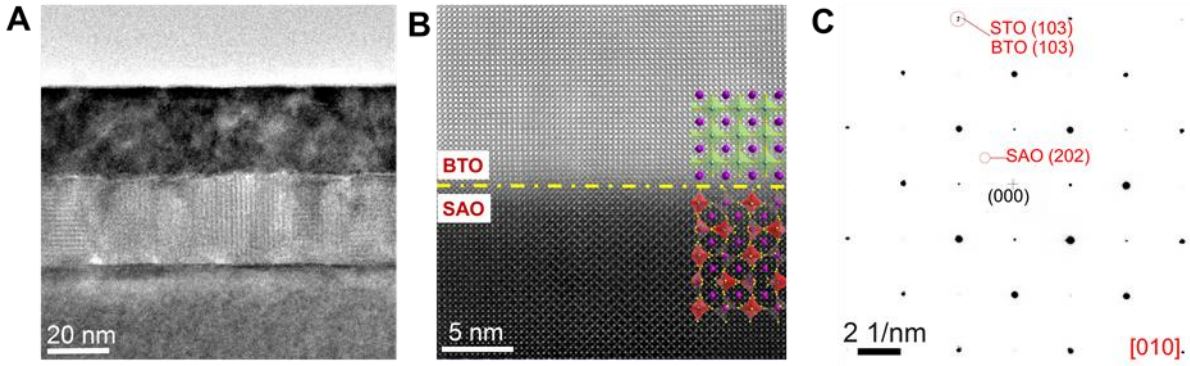

Fig. S6.

Microstructure of BTO/SAO/STO. (A) A cross-sectional TEM image of BTO/SAO/STO (001). **(B)** Magnified HAADF-STEM image and atomic model of the interface between BTO and SAO. **(C)** SAED pattern from the cross-sectional BTO/SAO/STO.

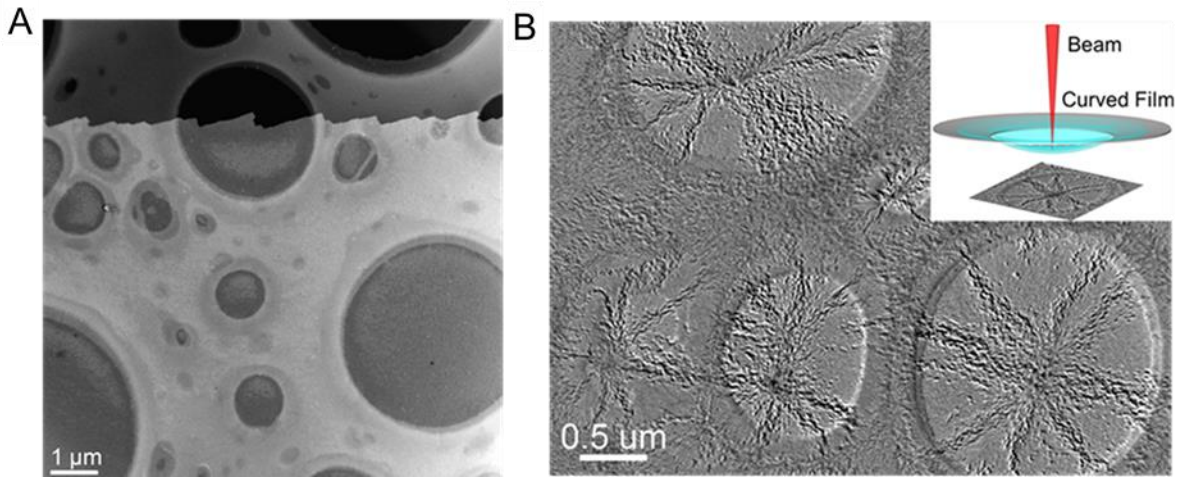

Fig. S7.

Morphology and structure of freestanding BTO. (A) Plane-viewed HAADF-STEM image of a freestanding BTO membrane supported by lacey carbon film. **(B)** A low-magnification TEM image of the freestanding BTO membrane with equal inclination fringes.

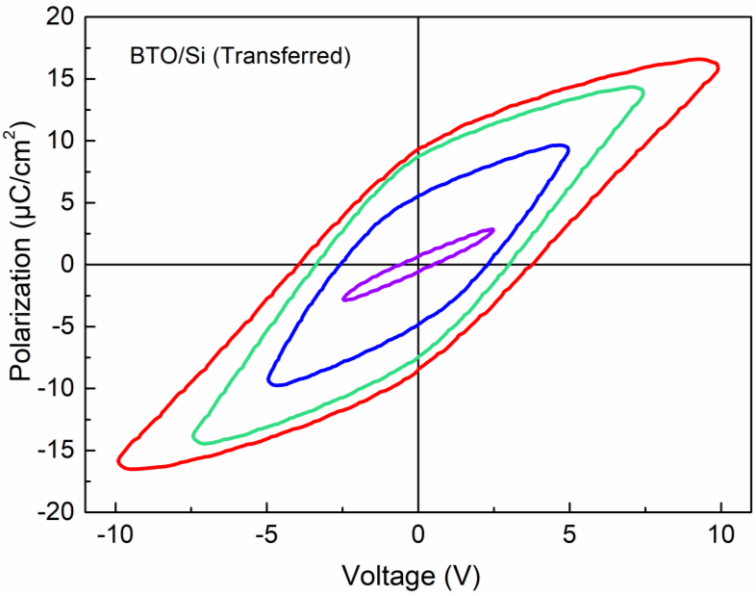

Fig. S8.

Ferroelectric properties. Polarization – voltage loops of the BTO membranes transferred on Pt/Si.

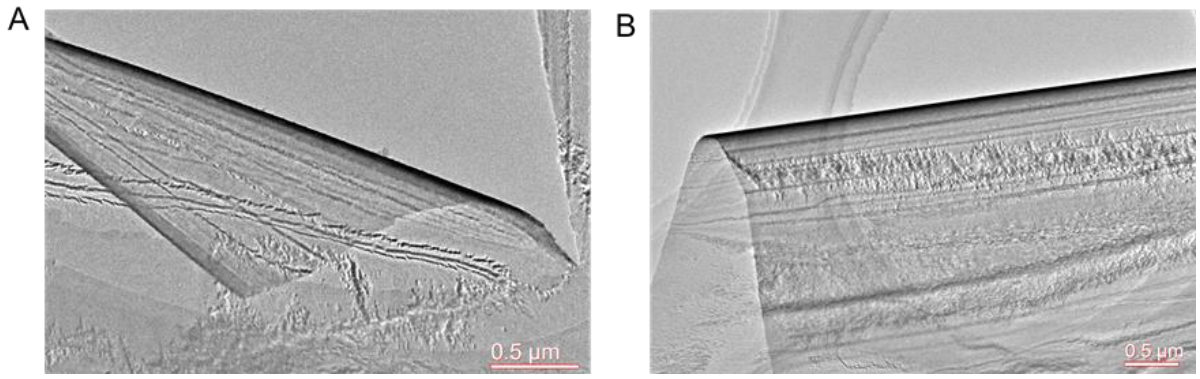

Fig. S9.

Morphology of folded freestanding BTO. (A-B) A low magnification TEM image of a freestanding BTO membrane with the folded and bent state. Remarkably, all these folded BTO membranes maintained integrity and continuity without any cracks, behaving more like a flexible organic film rather than brittle oxides

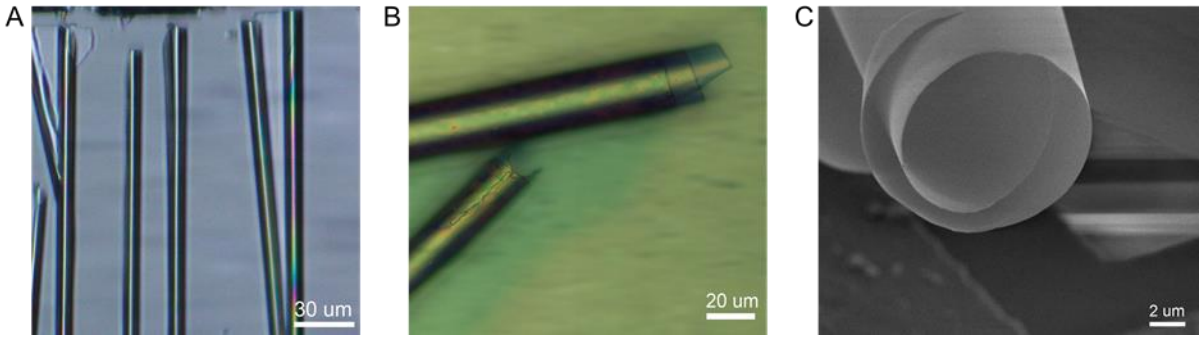

Fig. S10.

Morphology of the BTO rolls. (A-B) The optical photograph of BTO rolls. **(C)** SEM image of BTO roll. Through the design of the experiment, the freestanding BTO membranes were bent into several multi-layer rolls.

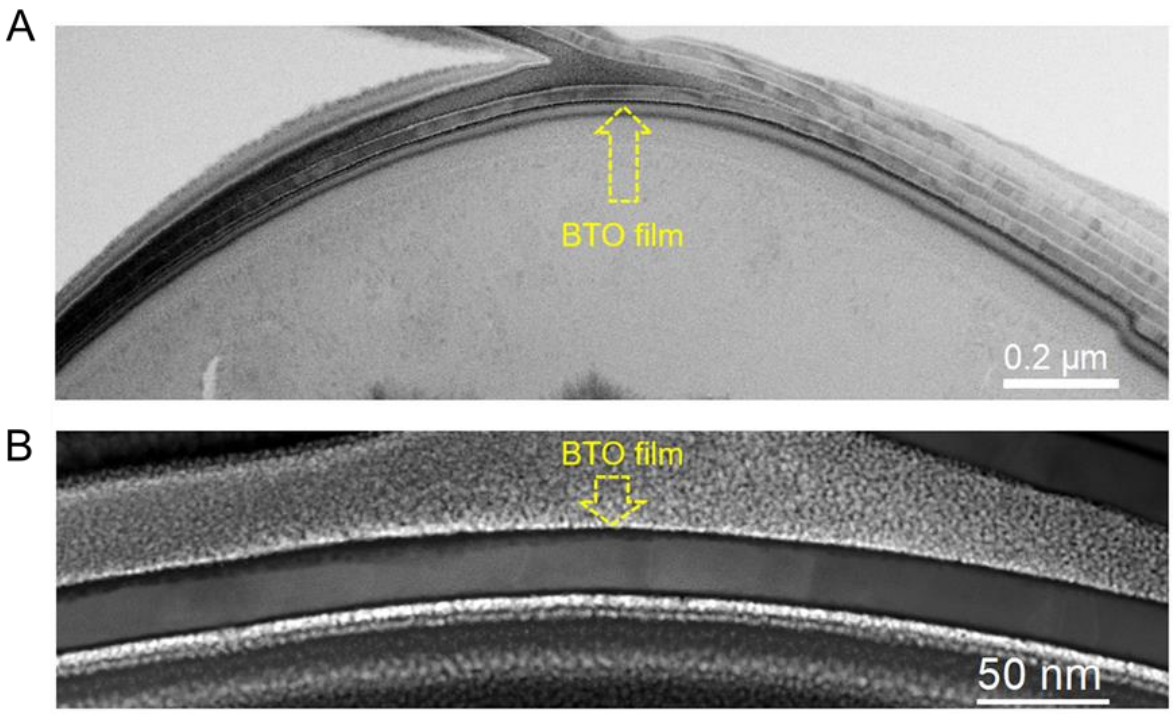

Fig. S11.

Structure of freestanding BTO with in a bent state. (A-B) Low-magnification cross-section STEM images of the bent freestanding BTO.

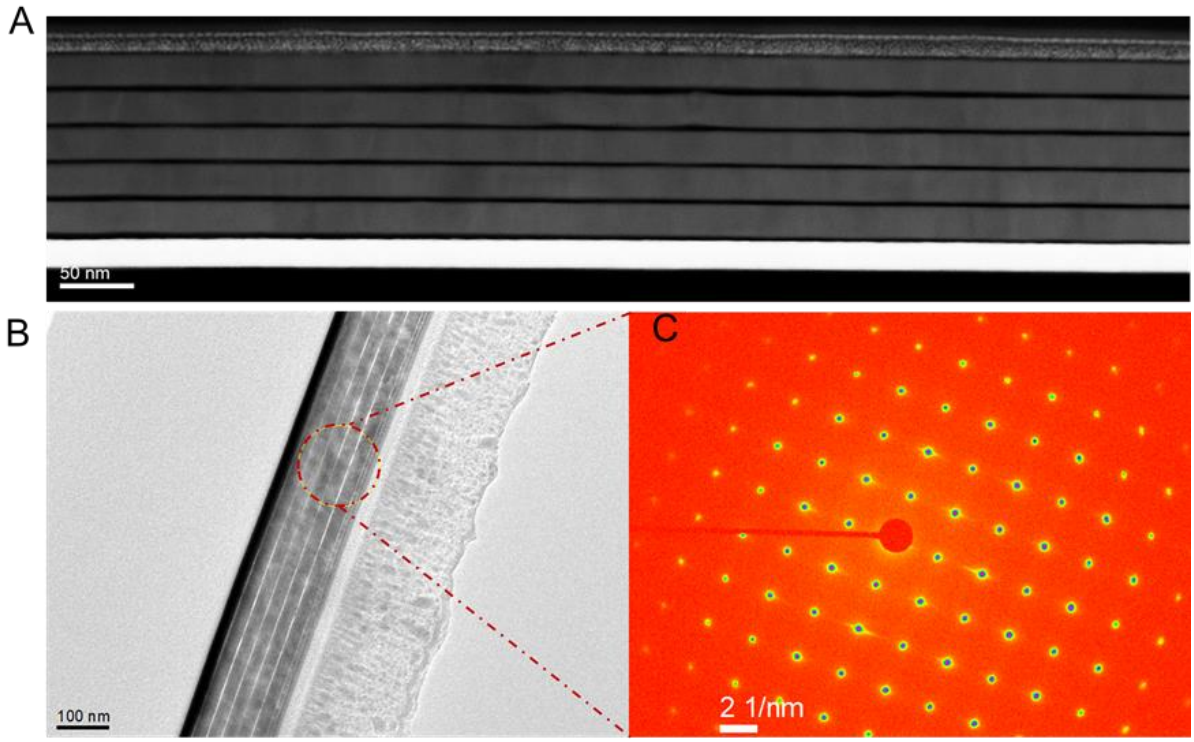

Fig. S12.

Structure of freestanding BTO multilayer. (A) Cross-sectional STEM image of freestanding BTO multilayer. **(B)** The cross-sectional TEM image of freestanding BTO multilayer. **(C)** SAED pattern from BTO multilayer in cross-section. The results indicate that all the layers have the same orientation.

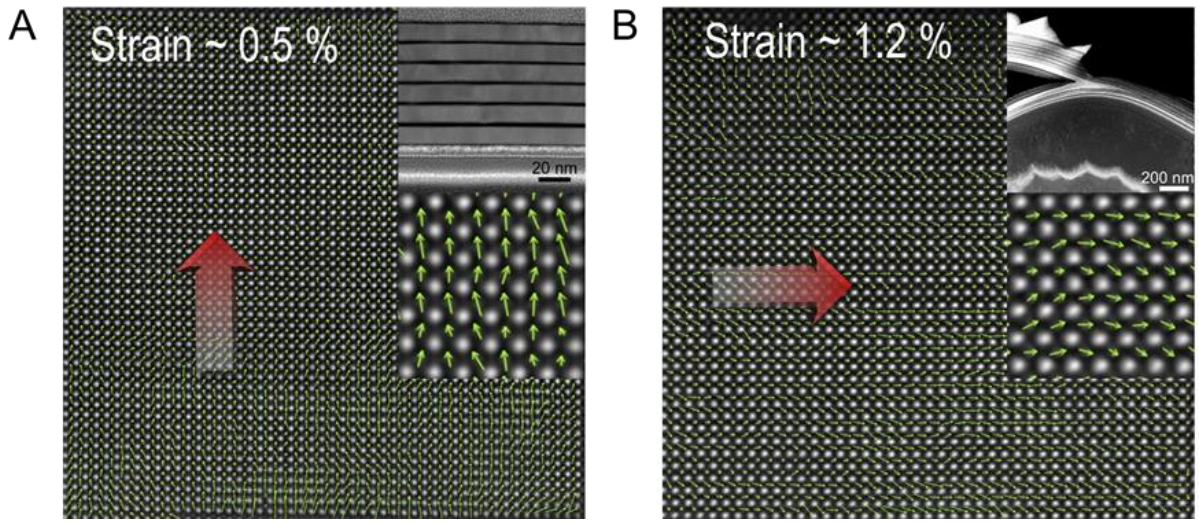

Fig. S13.

Reversed Ti^{4+} ion displacement vector. (A-B) Different strain conditions STEM images with the direction of polarization. The insert images show the representative polarized regions. The polarization orientations are correlated with the strain states.

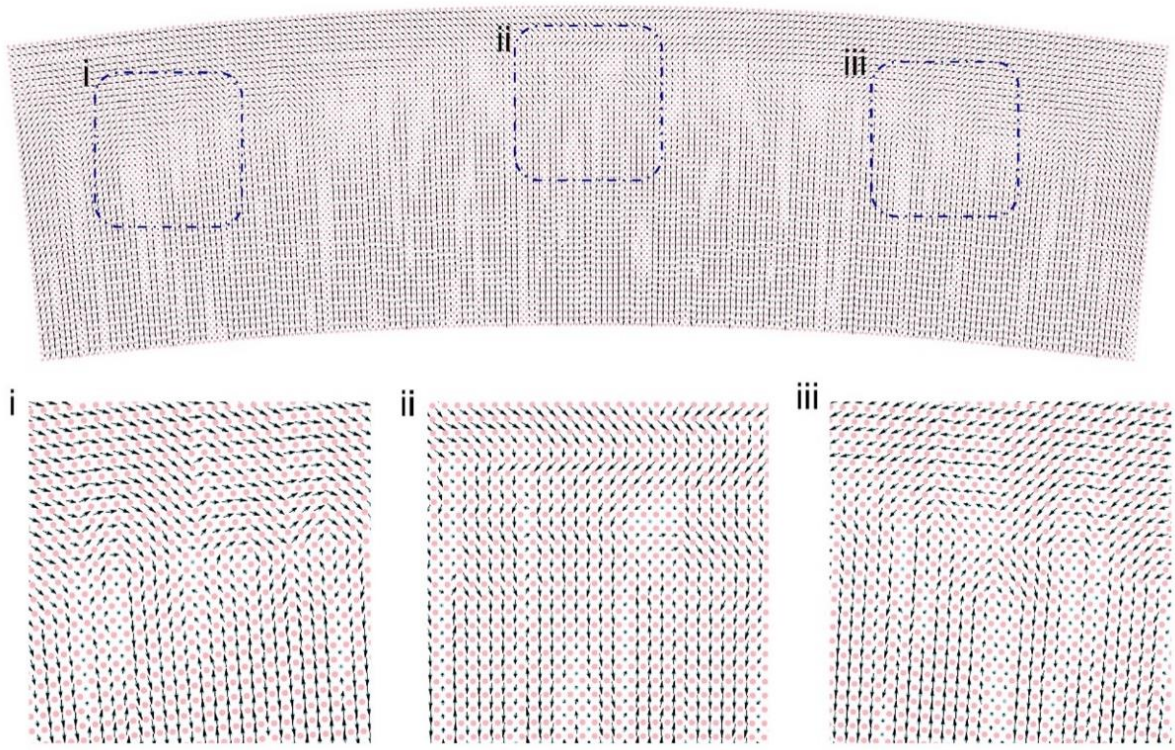

Fig. S14.

Atomistic simulations of the distribution of dipole configurations in a bent 20 nm-width $BaTiO_3$ membrane at ε_{max} = 3.1%. The bending deformation generates a stress gradient. Three typical regions (I, II, III) are selected to show the local polarizations. The arrow refers to the shift of displacement of Ti atoms from the center position in the unit lattice. Dipole displacements are amplified by a factor of 50 for clarity.

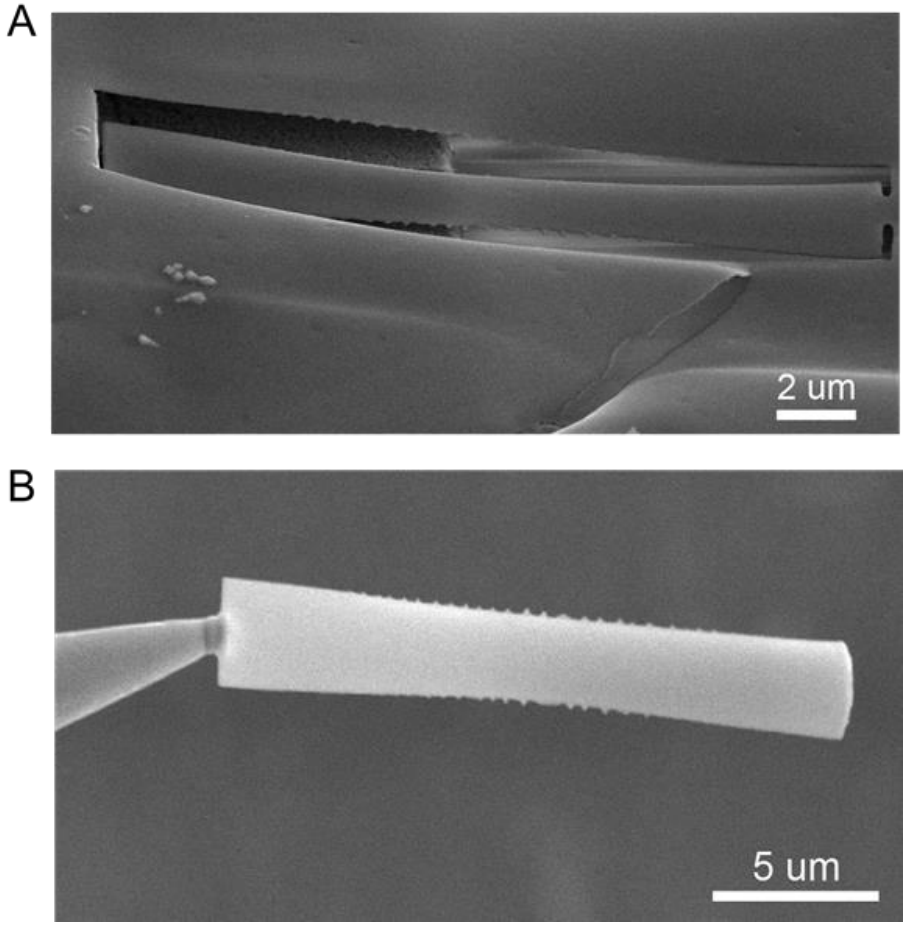

Fig. S15.

Morphology of BTO nano-belts. (A-B) The SEM images of freestanding BTO nano-belts. To further explore the mechanical behaviors of freestanding BTO membranes, we performed in-situ SEM manipulation of BTO nano-belts. Freestanding BTO nano-belts were fabricated by focused ion beam (FIB) and handled by the nano-manipulator tip in SEM.

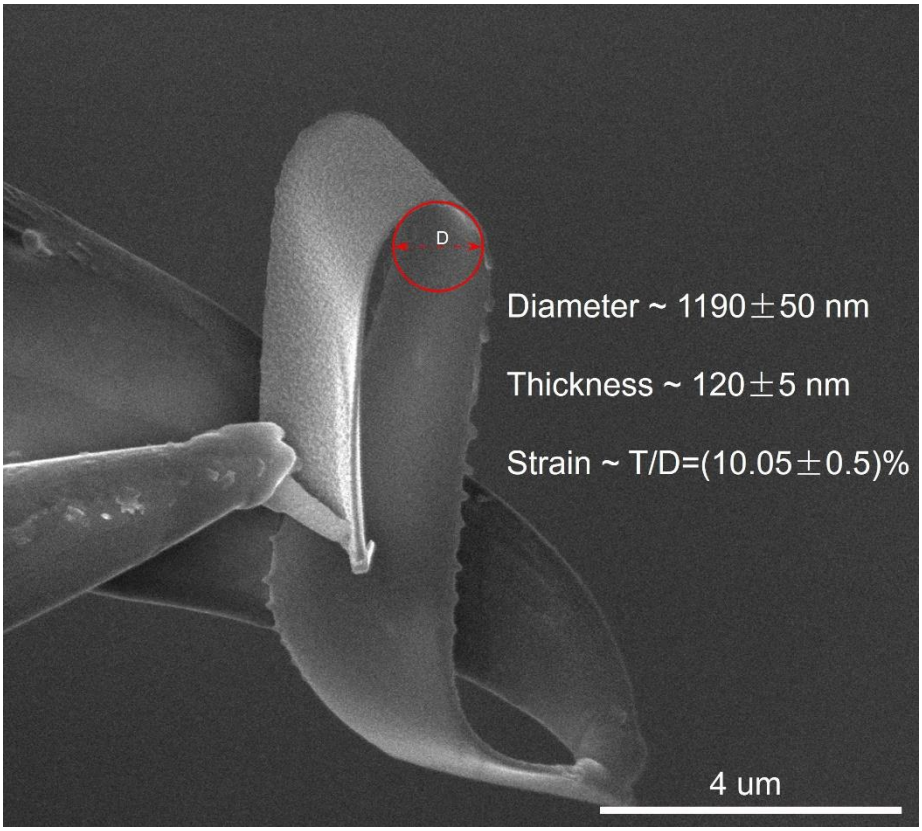

Fig. S16.

The calculation method for the strain of the BTO membrane during the bending process.

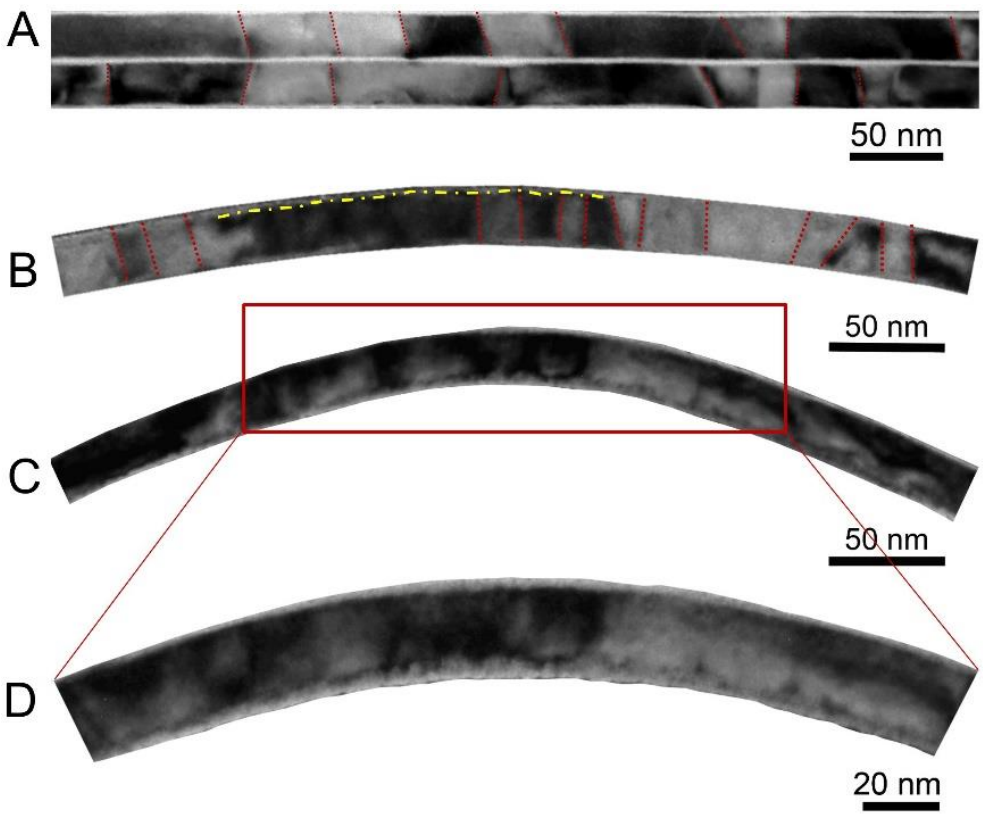

Fig. S17.

The domain architectures of BTO under different bent configurations. (A) TEM BF image of BTO at the horizontal (unbent) state. **(B)** TEM BF image of BTO at a slightly bent state. **(C)** TEM BF image of BTO at a bent state. **(D)** A magnified section of Fig. S17C.

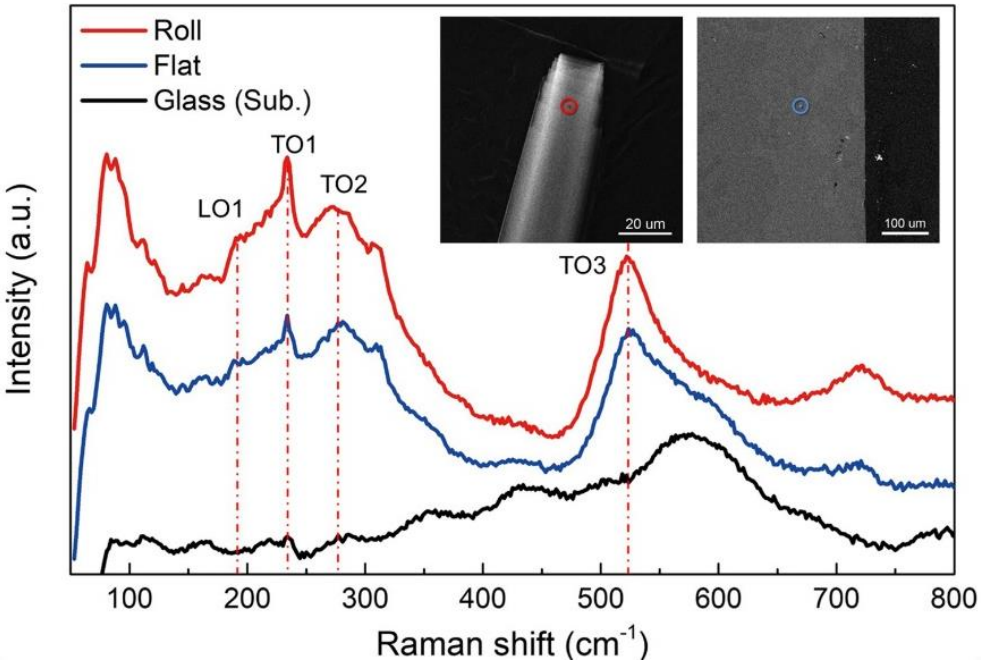

Fig. S18.

The Raman spectra of the flat and roll BTO membranes on glass substrates. The Raman spectra of BTO membrane and roll on glass substrates showing no structural phase transition in the BTO membranes under large curvatures. The insets show the two different feature locations at which the Raman spectra were measured.

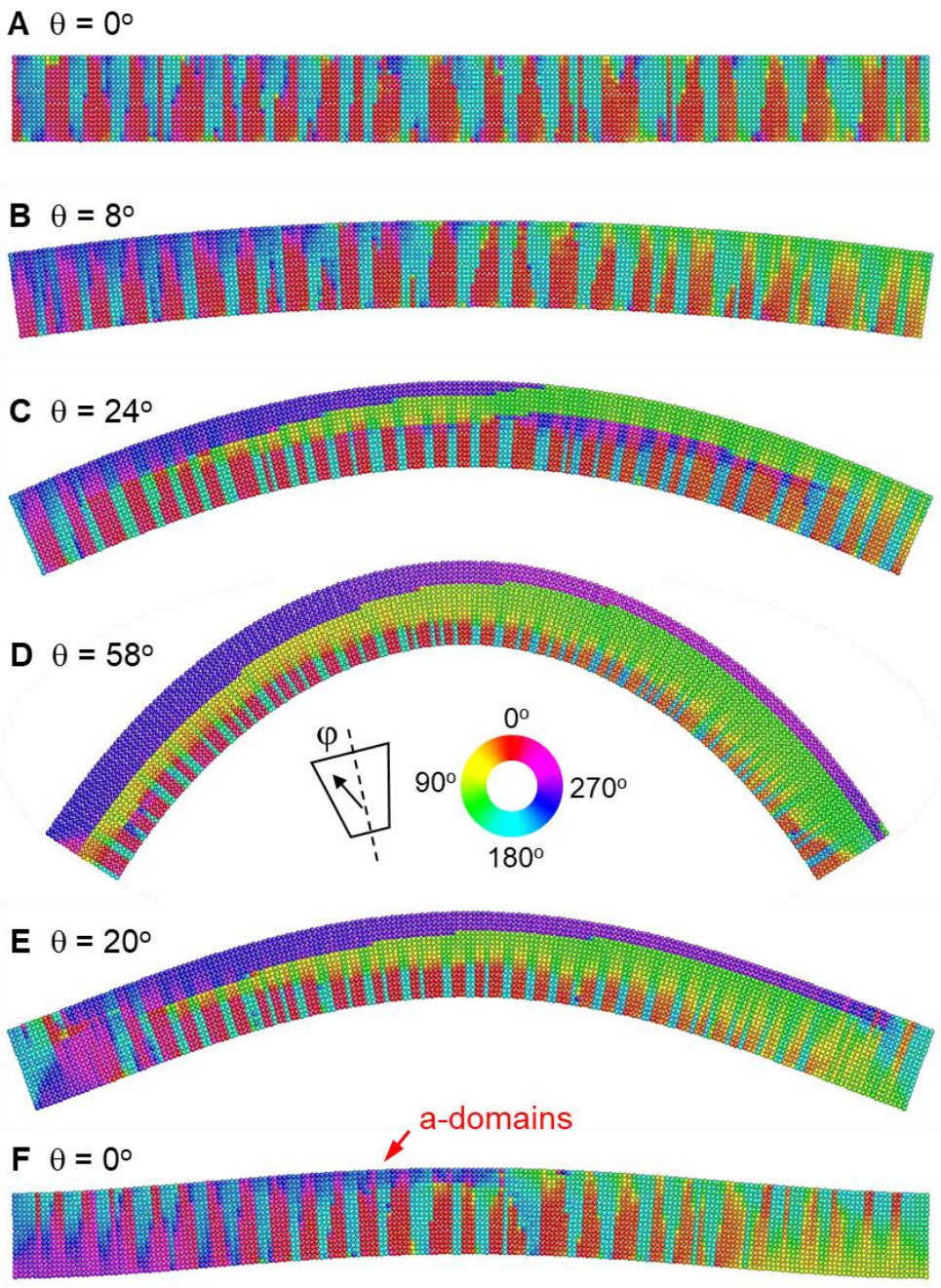

Fig. S19.

The typical snapshots of atomic configurations in $BaTiO_3$ membrane (*w* = 8 nm) at different bending angles upon the first loading/unloading cycle. The colors are coded according to the dipole rotation angle φ away from the central axis of the unit cell.

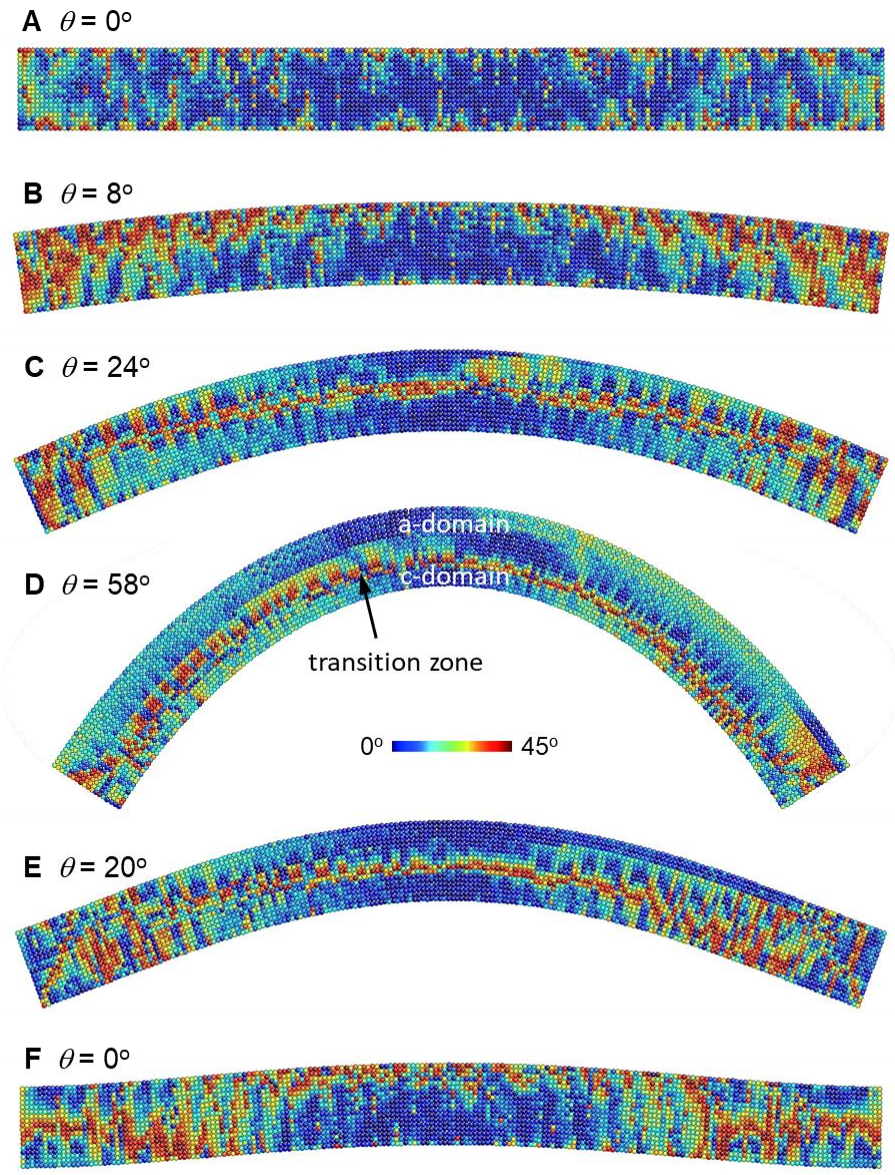

Fig. S20.

The distribution of deviation of dipole rotation η at different bending angles in sample with *w* = 8 nm at 300 K. The parameter η is defined as $\pi/4 - |\varphi - (n*\pi/2 + \pi/4)|$ for $\varphi \in [n*\pi/2, (n+1)*\pi/2]$, where φ is the rotation angle of polarization concerning the central axis in each unit cell and *n* runs from 0 to 3.

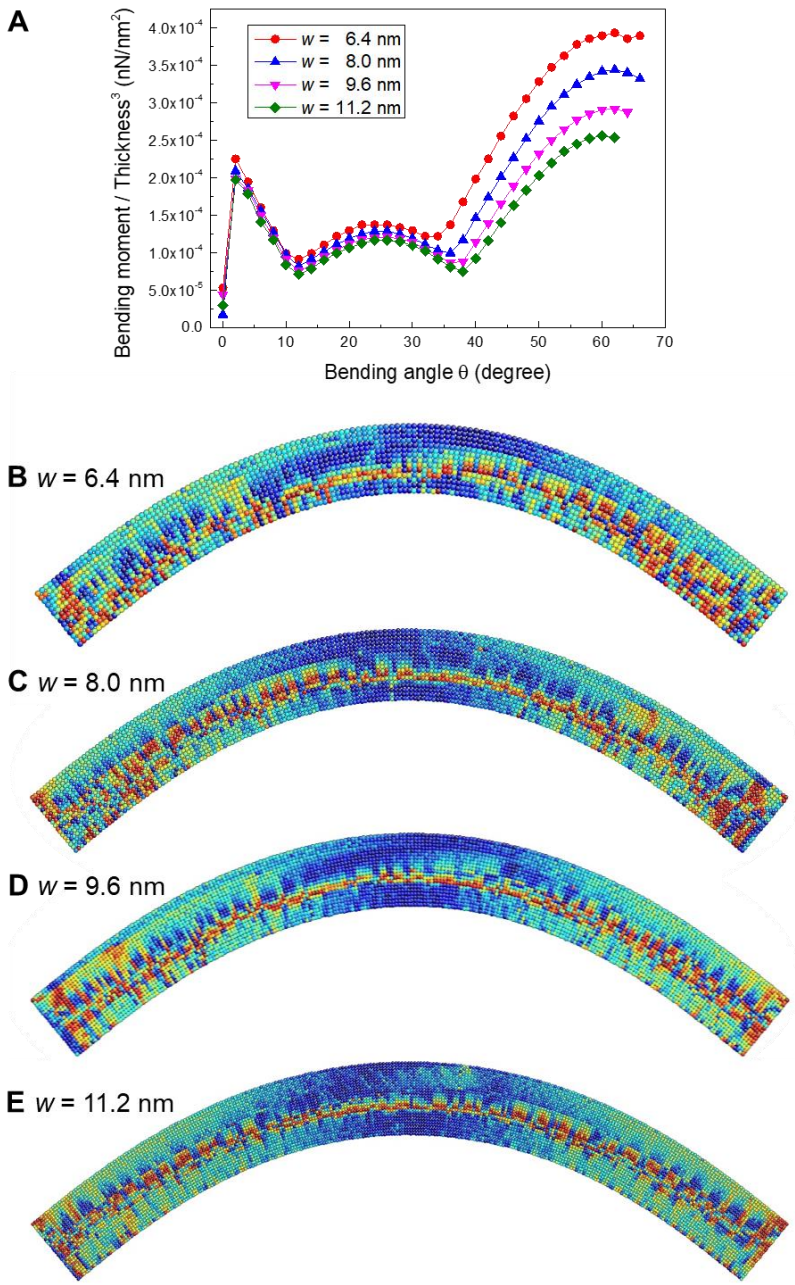

Fig. S21.

The size effect on super-elasticity. (A) The variation of effective stress (the moment divided by the thickness cubed) as the function of bending angle for the sample with a thickness ranging from 6.4 nm to 11.2 nm. **(B)-(E)** The spatial distribution of angle deviation η concerning the *a*- or *c*-domain for samples with different sizes at $\theta = 40^{o}$.

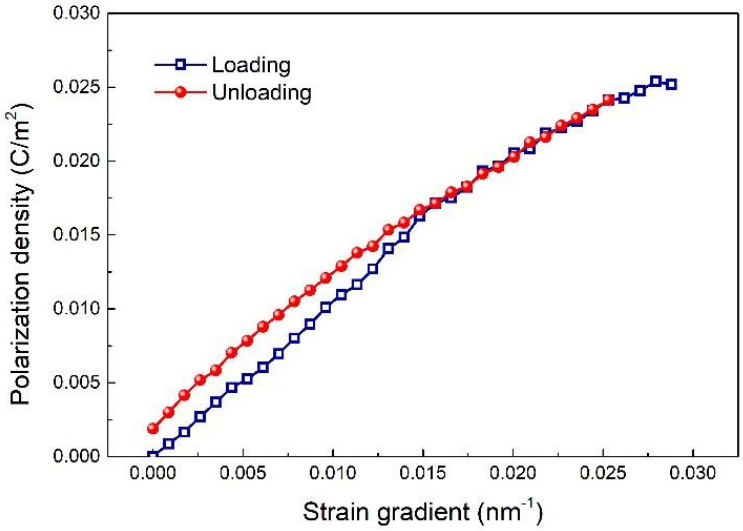

Fig. S22.

The variation of polarization density as the function of the strain gradient in sample with *w* = 8 nm at 300 K.

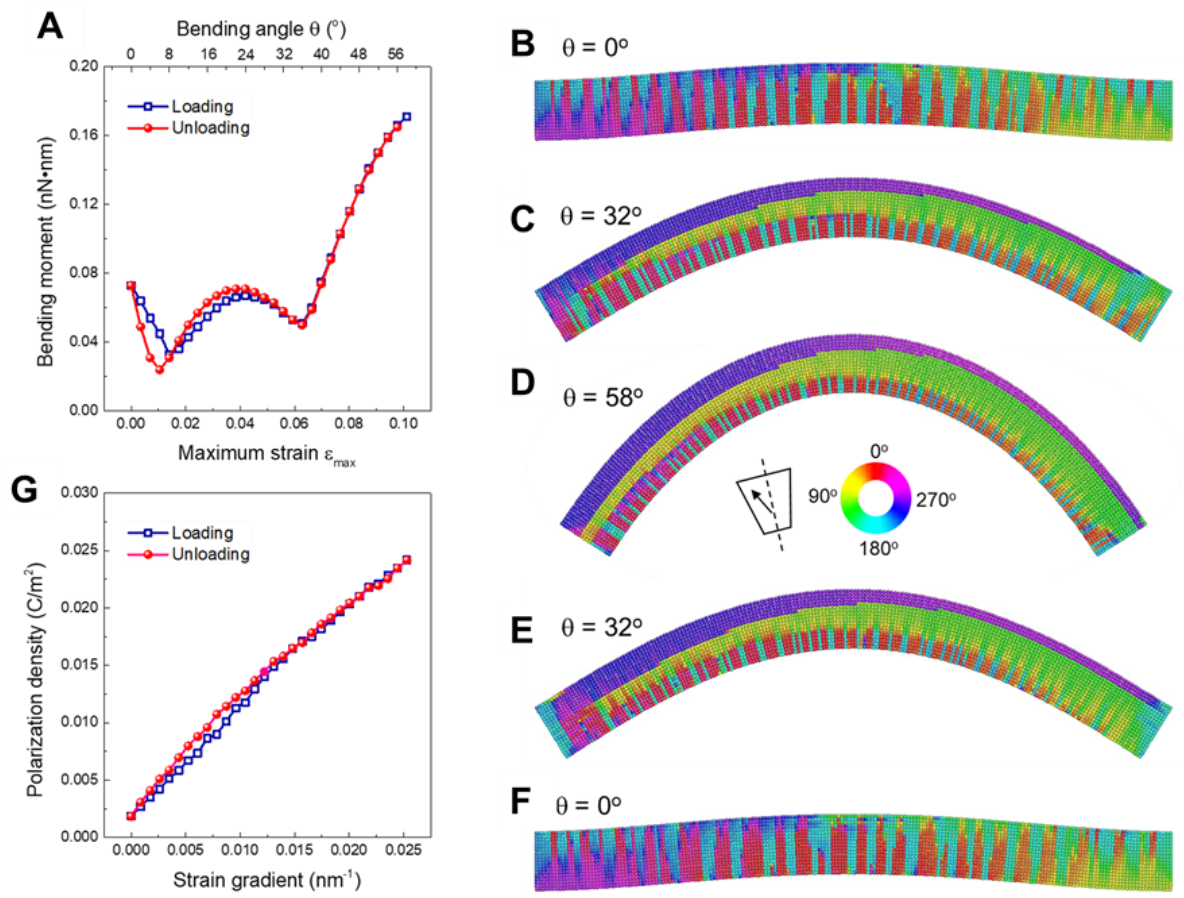

Fig. S23.

The second loading and unloading of $BaTiO_3$ membrane with w = 8 nm upon bending deformation at 300 K. (A) The variation of bending moment with bending angle θ (and maximum strain ε_{max}) under one loading/unloading cycle. **(B)-(F)** The typical snapshots of dipole configurations at different bending angles. The colors are coded according to the rotation angle concerning the c axis. **(G)** The variation of polarization density as the function of the strain gradient.

Movie S1.

In-situ SEM on a BTO nanobelt (20 μm×4 μm×120 nm) during the bending process (Fig. 3A is from this movie).

Movie S2.

In-situ SEM on a BTO nanobelt (20 μm×4 μm×60 nm) during the bending process (Fig. 3B is from this movie).

Movie S3.

In-situ SEM on a BTO nanobelt (20 μm×4 μm×30 nm) during the bending process.

Movie S4.

Typical snapshots of dipole configurations at different bending angles in the first loading/unloading cycle (Fig. 4B-E is taken from this movie).

Movie S5.

Typical snapshots of dipole rotation at different bending angles in the first loading/unloading cycle. The colors are coded according to the dipole rotation angle φ away from the central axis of the unit cell.

References and Notes

1. T. B. M. C. Barret, *Structure of Metals*, (Pergamon, Oxford, UK, 1992).

2. J. F. Gómez-Cortés, M. L. Nó, I. López-Ferreño, J. Hernández-Saz, S. I. Molina, A. Chuvilin, J. M. San Juan, Size effect and scaling power-law for superelasticity in shape-memory alloys at the nanoscale. *Nat. Nanotechnol.* **12**, 790–796 (2017).

3. G. Cheng, C. Miao, Q. Qin, J. Li, F. Xu, H. Haftbaradaran, E. C. Dickey, H. Gao, Y. Zhu, Large anelasticity and associated energy dissipation in single-crystalline nanowires. *Nat. Nanotechnol.* **10**, 687–691 (2015).

4. S. L. Wang, Z. W. Shan, H. Huang, The mechanical properties of nanowires. *Adv. Sci.* **4**, 24 (2017).

5. J. Cao, E. Ertekin, V. Srinivasan, W. Fan, S. Huang, H. Zheng, J. W. L. Yim, D. R. Khanal, D. F. Ogletree, J. C. Grossman, J. Wu, Strain engineering and one-dimensional organization of metal-insulator domains in single-crystal vanadium dioxide beams. *Nat. Nanotechnol.* **4**, 732–737 (2009).

6. A. Lai, Z. Du, C. L. Gan, C. A. Schuh, Shape memory and superelastic ceramics at small scales. *Science* **341**, 1505–1508 (2013).

7. T. Leydecker, M. Herder, E. Pavlica, G. Bratina, S. Hecht, E. Orgiu, P. Samorì, Flexible non-volatile optical memory thin-film transistor device with over 256 distinct levels based on an organic bicomponent blend. *Nat. Nanotechnol.* **11**, 769–775 (2016).

8. F. R. Fan, W. Tang, Z. L. Wang, Flexible Nanogenerators for Energy Harvesting and Self-Powered Electronics. *Adv. Mater.* **28**, 4283–4305 (2016).

9. Q. Zheng, B. J. Shi, Z. Li, Z. L. Wang, Recent progress on piezoelectric and triboelectric energy harvesters in biomedical systems. *Adv. Sci.* **4**, 23 (2017).

10. D. Lu, D. J. Baek, S. S. Hong, L. F. Kourkoutis, Y. Hikita, H. Y. Hwang, Synthesis of freestanding single-crystal perovskite films and heterostructures by etching of sacrificial water-soluble layers. *Nat. Mater.* **15**, 1255–1260 (2016).

11. S. R. Bakaul, C. R. Serrao, M. Lee, C. W. Yeung, A. Sarker, S.-L. Hsu, A. K. Yadav, L. Dedon, L. You, A. I. Khan, J. D. Clarkson, C. Hu, R. Ramesh, S. Salahuddin, Single crystal functional oxides on silicon. *Nat. Commun.* **7**, 10547 (2016).

12. L. Chang, L. You, J. L. Wang, The path to flexible ferroelectrics: Approaches and progress. *Jpn. J. Appl. Phys.* **57**, 7 (2018).

13. D. Ji, S. Cai, T. R. Paudel, H. Sun, C. Zhang, L. Han, Y. Wei, Y. Zang, M. Gu, Y. Zhang, W. Gao, H. Huyan, W. Guo, D. Wu, Z. Gu, E. Y. Tsymbal, P. Wang, Y. Nie, X. Pan, Freestanding crystalline oxide perovskites down to the monolayer limit. *Nature* **570**, 87–90 (2019).

14. Y. Qi, N. T. Jafferis, K. Lyons Jr., C. M. Lee, H. Ahmad, M. C. McAlpine, Piezoelectric ribbons printed onto rubber for flexible energy conversion. *Nano Lett.* **10**, 524–528 (2010).

15. Z. G. Zuo *et al*., Preparation and ferroelectric properties of freestanding Pb(Zr,Ti)O3 thin membranes. *J. Phys. D Appl. Phys.* **45**, 5 (2012).

16. L. Hong, A. K. Soh, Q. G. Du, J. Y. Li, Interaction of O vacancies and domain structures in single crystal BaTiO3: Two-dimensional ferroelectric model. *Phys. Rev. B Condens. Matter Mater. Phys.* **77**, 7 (2008).

17. S. Sahoo, S. Polisetty, C.-G. Duan, S. S. Jaswal, E. Y. Tsymbal, C. Binek, Ferroelectric control of magnetism in Ba Ti O 3 ⁄ Fe heterostructures via interface strain coupling. *Phys. Rev. B Condens. Matter Mater. Phys.* **76**, 092108 (2007).

18. Materials and methods are available as supplementary materials.

19. C. Dubourdieu, J. Bruley, T. M. Arruda, A. Posadas, J. Jordan-Sweet, M. M. Frank, E. Cartier, D. J. Frank, S. V. Kalinin, A. A. Demkov, V. Narayanan, Switching of ferroelectric polarization in epitaxial BaTiO3 films on silicon without a conducting bottom electrode. *Nat. Nanotechnol.* **8**, 748–754 (2013).

20. E. Spiecker, Determination of crystal polarity from bend contours in transmission electron microscope images. *Ultramicroscopy* **92**, 111–132 (2002).

21. J. L. Rouvière, E. Sarigiannidou, Theoretical discussions on the geometrical phase analysis. *Ultramicroscopy* **106**, 1–17 (2005).

22. I. Stolichnov, L. Feigl, L. J. McGilly, T. Sluka, X.-K. Wei, E. Colla, A. Crassous, K. Shapovalov, P. Yudin, A. K. Tagantsev, N. Setter, Bent Ferroelectric Domain Walls as Reconfigurable Metallic-Like Channels. *Nano Lett.* **15**, 8049–8055 (2015).

23. Z. B. Chen, L. Hong, F. F. Wang, S. P. Ringer, L. Q. Chen, H. S. Luo, X. Z. Liao, Facilitation of ferroelectric switching via mechanical manipulation of hierarchical nanoscale domain structures. *Phys. Rev. Lett.* **118**, 7 (2017).

24. T. D. Nguyen, S. Mao, Y. W. Yeh, P. K. Purohit, M. C. McAlpine, Nanoscale flexoelectricity. *Adv. Mater.* **25**, 946–974 (2013).

25. W. J. Chen, Y. Zheng, X. Feng, B. Wang, Utilizing mechanical loads and flexoelectricity to induce and control complicated evolution of domain patterns in ferroelectric nanofilms. *J. Mech. Phys. Solids* **79**, 108–133 (2015).

26. Y. Tanaka, Y. Himuro, R. Kainuma, Y. Sutou, T. Omori, K. Ishida, Ferrous polycrystalline shape-memory alloy showing huge superelasticity. *Science* **327**, 1488–1490 (2010).

27. J. San Juan, M. L. Nó, C. A. Schuh, Nanoscale shape-memory alloys for ultrahigh mechanical damping. *Nat. Nanotechnol.* **4**, 415–419 (2009).

28. D. D. Viehland, E. K. H. Salje, Domain boundary-dominated systems: Adaptive structures and functional twin boundaries. *Adv. Phys.* **63**, 267–326 (2014).

29. Y. M. Jin, Y. U. Wang, A. G. Khachaturyan, J. F. Li, D. Viehland, Adaptive ferroelectric states in systems with low domain wall energy: Tetragonal microdomains. *J. Appl. Phys.* **94**, 3629–3640 (2003).

30. D. Viehland, Symmetry-adaptive ferroelectric mesostates in oriented Pb(BI[sub 1/3]BII[sub 2/3])O[sub 3]–PbTiO[sub 3] crystals. *J. Appl. Phys.* **88**, 4794–4806 (2000).

31. Y. M. Jin, Y. U. Wang, A. G. Khachaturyan, J. F. Li, D. Viehland, Conformal miniaturization of domains with low domain-wall energy: Monoclinic ferroelectric states near the morphotropic phase boundaries. *Phys. Rev. Lett.* **91**, 4 (2003).

32. G. De Luca, M. D. Rossell, J. Schaab, N. Viart, M. Fiebig, M. Trassin, Domain Wall Architecture in Tetragonal Ferroelectric Thin Films. *Adv. Mater.* **29**, 1605145 (2017).

33. S. Cherifi-Hertel, H. Bulou, R. Hertel, G. Taupier, K. D. H. Dorkenoo, C. Andreas, J. Guyonnet, I. Gaponenko, K. Gallo, P. Paruch, Non-Ising and chiral ferroelectric domain walls revealed by nonlinear optical microscopy. *Nat. Commun.* **8**, 15768 (2017).

34. G. Catalan, A. Lubk, A. H. G. Vlooswijk, E. Snoeck, C. Magen, A. Janssens, G. Rispens, G. Rijnders, D. H. A. Blank, B. Noheda, Flexoelectric rotation of polarization in ferroelectric thin films. *Nat. Mater.* **10**, 963–967 (2011).

35. D. A. Cogswell, M. Z. Bazant, Size-dependent phase morphologies in LiFePO4 battery particles. *Electrochem. Commun.* **95**, 33–37 (2018).

36. Z. Zhang, X. D. Ding, J. Sun, T. Suzuki, T. Lookman, K. Otsuka, X. B. Ren, Nonhysteretic superelasticity of shape memory alloys at the nanoscale. *Phys. Rev. Lett.* **111**, 5 (2013).

37. D. A. Cogswell, M. Z. Bazant, Theory of coherent nucleation in phase-separating nanoparticles. *Nano Lett.* **13**, 3036–3041 (2013).

38. Y. J. Gu, M. L. Li, A. N. Morozovska, Y. Wang, E. A. Eliseev, V. Gopalan, L. Q. Chen, Flexoelectricity and ferroelectric domain wall structures: Phase-field modeling and DFT calculations. *Phys. Rev. B Condens. Matter Mater. Phys.* **89**, 11 (2014).

39. Y. L. Li, L. Q. Chen, Temperature-strain phase diagram for BaTiO3 thin films. *Appl. Phys. Lett.* **88**, 3 (2006).

40. J. M. Vielma, G. Schneider, Shell model of BaTiO3 derived from ab-initio total energy calculations. *J. Appl. Phys.* **114**, 174108 (2013).

41. B. He, B. Javvaji, X. Y. Zhuang, Size dependent flexoelectric and mechanical properties of barium titanate nanobelt: A molecular dynamics study. *Physica B* **545**, 527–535 (2018).

42. S. Tinte, M. G. Stachiotti, S. R. Phillpot, M. Sepliarsky, D. Wolf, R. L. Migoni, Ferroelectric properties of BaxSr1-xTiO3 solid solutions obtained by molecular dynamics simulation. *J. Phys. Condens. Matter* **16**, 3495–3506 (2004).

43. S. Nosé, A unified formulation of the constant temperature molecular-dynamics methods. *J. Chem. Phys.* **81**, 511–519 (1984).

44. S. Plimpton, Fast parallel algorithms for short-range molecular-dynamics. *J. Comput. Phys.* **117**, 1–19 (1995).

45. J. Li, AtomEye: An efficient atomistic configuration viewer. *Model. Simul. Mater. Sci. Eng.* **11**, 173–177 (2003).

46. L. Q. Chen, Phase-field method of phase transitions/domain structures in ferroelectric thin films: A review. *J. Am. Ceram. Soc.* **91**, 1835–1844 (2008).

47. N. Shibata, S. D. Findlay, Y. Kohno, H. Sawada, Y. Kondo, Y. Ikuhara, Differential phase-contrast microscopy at atomic resolution. *Nat. Phys.* **8**, 611–615 (2012).

48. P. Zubko, G. Catalan, A. Buckley, P. R. L. Welche, J. F. Scott, Strain-gradient-induced polarization in SrTiO3 single crystals. *Phys. Rev. Lett.* **99**, 167601 (2007).

49. W. H. Ma, L. E. Cross, Flexoelectricity of barium titanate. *Appl. Phys. Lett.* **88**, 232902 (2006).

50. R. Maranganti, P. Sharma, Atomistic determination of flexoelectric properties of crystalline dielectrics. *Phys. Rev. B Condens. Matter Mater. Phys.* **80**, 054109 (2009).

51. M. Stengel, Surface control of flexoelectricity. *Phys. Rev. B Condens. Matter Mater. Phys.* **90**, 201112 (2014).